Journal of Colloid and Interface Science 703 (2026) 139183

Contents lists available at ScienceDirect

Journal of Colloid And Interface Science

journal homepage: www.elsevier.com/locate/jcis

Tumor-targeting Cu^{2+}/IR820-rich nanozymes to exert photothermal-reinforced reactive oxygen species production and dual glutathione scavenging for synergistic cancer therapy

Hsiang-Yun Chih [a], I-Ju Liu [a], Tzu-Chen Lin [a], Shang-Hsiu Hu [b], Tsai-Ching Hsu [c,d,e], Ju-An Liang [c], Chia-Wei Kuo [c], Bor-Show Tzang [c,d,e,f,**], Wen-Hsuan Chiang [a,g,*]

[a] Department of Chemical Engineering, National Chung Hsing University, Taichung 402, Taiwan
[b] Department of Biomedical Engineering and Environmental Sciences, National Tsing Hua University, Hsinchu 300, Taiwan
[c] Institute of Medicine, Chung Shan Medical University, Taichung 402, Taiwan
[d] Immunology Research Center, Chung Shan Medical University, Taichung 402, Taiwan
[e] Department of Clinical Laboratory, Chung Shan Medical University Hospital, Taichung 402, Taiwan
[f] Department of Biochemistry, School of Medicine, Chung Shan Medical University, Taichung 402, Taiwan
[g] i-Center for Advanced Science and Technology (iCAST), National Chung Hsing University, Taichung 402, Taiwan

GRAPHICAL ABSTRACT

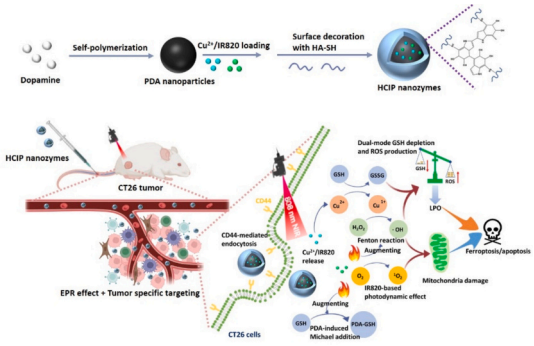

ARTICLE INFO

Keywords:
Tumor-targeting nanozymes
Dual GSH depletion
Photothermal-boosted ROS production
ROS-mediated tumor treatment
Cu^{2+} ions
IR820

ABSTRACT

Despite the remarkable progress in reactive oxygen species (ROS)-mediated tumor treatment based on catalytic therapy and photodynamic therapy, the high intracellular glutathione (GSH) level, low Fenton reaction efficacy, and poor tumor targeting of small-molecule photosensitizers largely restrict the ROS-based antitumor effect. To overcome these challenges in better tumor treatment, versatile tumor-targeting nanozymes capable of conducting photothermal-reinforced GSH consumption and ROS production were fabricated through the incorporation of Cu^{2+} ions and IR820 with hyaluronic acid (HA)-decorated polydopamine (PDA) nanoparticles. The resulting HA-coated Cu^{2+}/IR820@PDA (HCIP) nanozymes exhibited a solid-like spherical shape, sound colloidal dispersion, acid-activated Cu^{2+} and IR820 release. These nanozymes not only showed outstanding photothermal

* Corresponding author at: Department of Chemical Engineering, National Chung Hsing University, Taichung 402, Taiwan.
** Corresponding author at: Institute of Medicine, Chung Shan Medical University, Taichung 402, Taiwan.
E-mail addresses: bstzang@csmu.edu.tw (B.-S. Tzang), whchiang@dragon.nchu.edu.tw (W.-H. Chiang).

https://doi.org/10.1016/j.jcis.2025.139183
Received 24 June 2025; Received in revised form 2 October 2025; Accepted 3 October 2025
Available online 8 October 2025

conversion efficiency (42.5 %), photothermal-enhanced PDA/Cu^{2+}-elicited dual-mode GSH depletion and Cu^{2+}-mediated hydroxyl radical (·OH) production, but also produced sufficient singlet oxygen ($^1O_2$) via IR820-based photodynamic effect. After being internalized by CT26 colon cancer cells via CD44-mediated endocytosis, the HCIP nanozymes efficiently depleted endogenous GSH and generated massive ROS comprising ·OH and $^1O_2$ as well as hyperthermia under near-infrared (NIR) laser irradiation, thereby promoting apoptosis and ferroptosis via mitochondrial damage and lipid peroxidation. Notably, the in vivo studies showed that the HCIP nanozymes effectively accumulated at the CT26 tumor sites and inhibited tumor growth and splenomegaly upon photothermal-boosted ROS-mediated anticancer efficacy combined with ferroptosis without severe side effects. This work provides a new strategy for the design of dual-mode GSH-depleting and ROS-producing nanozymes to realize synergistic tumor treatment.

1. Introduction

Cancer poses a significant threat to human health, prompting the development of various strategies to promote clinical efficiency [1–3]. Among the most studied approaches are exogenous-triggered photodynamic therapy (PDT) and endogenous-responsive catalytic therapy, both of which have been demonstrated to effectively induce cell apoptosis and ferroptosis by generating singlet oxygen ($^1O_2$) and hydroxyl radicals (•OH) [3–6]. The production of $^1O_2$ is influenced by oxygen (O_2) concentration, while the generation of •OH is primarily determined by the types of nanozymes used [3]. In general, excessive reactive oxygen species (ROS), such as •OH, $^1O_2$, and superoxide anions ($O_2^{\bullet-}$), can irreversibly oxidize and damage essential cellular biomacromolecules like proteins, lipids, and DNA, leading to cancer cell apoptosis and/or ferroptosis [3–9]. To further enhance the antitumor potency of the ROS-mediated therapy, the integration of catalytic therapy and PDT, capable of enhancing intracellular toxic $^1O_2$ and •OH accumulation, has emerged as a potential strategy [10–14]. Although promising, the combination of catalytic therapy and PDT still encounters several critical challenges that hinder its practical application. In addition to poor photostability and non-tumor targeting of small-molecule photosensitizers, tumor hypoxia remarkably reduced the anticancer effect of O_2-dependent PDT [15,16]. Also, the high levels of glutathione (GSH) (ranging from 2 to 10 mM) act as a scavenger of ROS, keeping the redox homeostasis in cancer cells, which in turn reduces the effectiveness of catalytic therapy and PDT [16–18].

In the past decade, nanozymes with inherent enzyme-like properties have garnered significant attention due to their desirable catalytic activity, sound stability, low cost, and ease of preparation [19,20]. A variety of nanozymes, such as metal oxides [21,22], carbon nanomaterials [23,24], and metal-organic frameworks (MOFs) [3,9,10,17,18], have been created and found to mimic various enzyme activities, including catalase (CAT), peroxidase (POD), and glucose oxidase (GOx). The nanozymes with POD-like activity can convert intracellular H_2O_2 into toxic •OH based on Fenton or Fenton-like reaction, which elicit cell death and are thus extensively utilized in catalytic therapy. Various multivalent metal ion pairs, including Cu^+/Cu^{2+} [1,9,10], Fe^{2+}/Fe^{3+} [12,13,17,18], and Mn^{2+}/Mn^{3+} [25], serving as Fenton or Fenton-like agents, have been employed as essential components of nanozymes for catalytic therapy. Some studies reported that Cu^+-mediated Fenton-like reactions can occur in weakly acidic or neutral environments, and the reaction rate ($1 \times 10^4\ M^{-1}\ s^{-1}$) is approximately 160 times faster than that of the Fe^{2+}-catalyzed Fenton reaction [26,27]. Also, the valence transition between Cu^{2+} and Cu^+ has been demonstrated to deplete intracellular GSH effectively [9,27–29]. In view of the above findings, several Cu^{2+}/Cu^+-containing nanozymes have been developed for cancer catalytic therapy [1,9,30]. Note that the concentration of free copper must remain below one atom per cell to prevent severe systemic toxicity [27]. Therefore, for Cu^+-mediated catalytic therapy to be safe and effective, free copper ions must be confined to tumor cells while remaining in a non-free ionic form during the blood circulation. To this end, it is essential to endow the Cu^{2+}/Cu^+-rich nanozymes with active tumor-targeting capability and controlled copper ion release.

Polydopamine (PDA) nanoparticles that can convert near-infrared (NIR) light into heat through a non-radiative procedure used as a photothermal conversion agent of photothermal therapy (PTT) to treat cancer and wound infection have received substantial attention due to several superior properties, including outstanding biocompatibility, strong chelation with various transition metal ions, and non-long-term toxicity [31–33]. Also, it should be mentioned that PDA has a large number of α,β-unsaturated carbonyl groups, thus irreversibly reacting with thiols by the Michael addition reaction in a mild milieu [34,35]. This can facilitate intracellular GSH depletion to increase the ROS level. Furthermore, the increased studies revealed that the photothermal effect can effectively boost the catalytic activity of nanozymes [3,19,36,37]. Several studies have reported that the delivery of Cu^{2+} ions or photosensitizers by PDA-based nanoparticles to achieve combination cancer therapy [27,34]. These therapeutic nanoparticles are often functionalized with hydrophilic poly(ethylene glycol) (PEG) to improve colloidal stability; however, the internalization of PEGylated nanoparticles by cancer cells is remarkably hindered, potentially reducing their anticancer efficacy. Additionally, to the best of our knowledge, there have been rare studies investigating the tumor-targeted co-delivery of Cu^{2+} ions and photosensitizers by PDA-based nanoparticles for synergistic PTT-enhanced catalytic therapy and PDT. Based on the above viewpoints, it is worth developing PDA nanoparticles decorated with hydrophilic and tumor-targeting functionalized surfaces to deliver both Cu^{2+} ions and photosensitizers for realizing effective tumor treatment by tumor-specific photothermal-augmented catalytic therapy and PDT.

Herein, we fabricate the active tumor-targeting PDA nanoparticles for co-delivery of Cu^{2+} and IR820, a photosensitizer, to boost antitumor potency by photothermal-augmented catalytic therapy and PDT. First, through the self-polymerization of dopamine monomers, the PDA nanoparticles were prepared and then coordinated with Cu^{2+} and laden with IR820 via π-π stacking and hydrophobic interactions. Due to the catalytic activity of Cu^{2+} ions, the Cu^{2+}-containing nanoparticles can be considered as nanozymes. Subsequently, the thiol-modified hyaluronic acid (HA-SH) segments were decorated onto the surfaces of Cu^{2+}/IR820@PDA nanozymes via Michael addition, yielding HA-Cu^{2+}/IR820@PDA (HCIP) nanozymes with active targeting capability toward CD44 receptors, which are overexpressed in various cancer cells. The HCIP nanozymes were characterized to have a uniform solid-like spherical shape and satisfied Cu^{2+} and IR820 loading capability. The HCIP nanozymes stabilized by hydrophilic HA coating displayed sound colloidal dispersion in pH 7.4 serum-containing aqueous solutions and accelerated Cu^{2+} and IR820 liberation under weakly acidic conditions mimicking acidic organelles. Also, these nanozymes not only showed prominent photothermal conversion efficiency (42.5 %), PDA/Cu^{2+}-elicited dual-mode GSH depletion and photothermal-enhanced Cu^{2+}-mediated ·OH production, but also generated sufficient $^1O_2$ via IR820-based photodynamic effect. After being internalized by CT26 colon cancer cells via CD44-mediated endocytosis, the HCIP nanozymes significantly depleted endogenous GSH and produced enormous ROS composed of ·OH and $^1O_2$ as well as hyperthermia under NIR laser irradiation, thus provoking mitochondrial damage and lipid peroxidation (LPO) to lead to apoptosis and ferroptosis. Notably, the in vivo studies demonstrated that the HCIP nanozymes effectively accumulated at the CT26 tumor sites and inhibited tumor growth and splenomegaly

via photothermal-boosted PDT/catalytic therapy combined with ferroptosis without severe side effects. This work provides a new horizon for rationally designing versatile nanozymes with dual-mode GSH depletion and ROS production, promising manifest progress in tumor treatment.

2. Experimental section

2.1. Materials and reagents

Copper (II) chloride dihydrate ($CuCl_2 \cdot 2H_2O$, ≧99 %) was obtained from SHOWA (Japan). IR820 (80 %), propidium iodide (PI, ≧94 %), 2′,7′-dichlorodihydrofluorescein diacetate (DCFH-DA, ≧97 %), 3-(4,5-Dimethylthiazol-2-yl)-2,5-diphenyltetrazolium bromide (MTT, 98 %), 1,3-diphenylisobenzofuran (DPBF, 97 %), and Roswell Park Memorial Institute (RPMI) 1640 medium were obtained from Sigma-Aldrich (USA). N-(3-Dimethylaminopropyl)-N′-ethylcarbodiimide hydrochloride (EDC, 95 %) was obtained from Matrix Scientific (USA). Dopamine hydrochloride (DA·HCl, 99 %), N-hydroxysuccinimide (NHS, 98 %), and bathocuproin sulfonate disodium salt hydrate (BCS, 97 %) were acquired from Alfa Aesar (USA). 2,2′-Azino-bis(3-ethylbenzothiazoline-6-sulfonic acid) (ABTS, 95 %) was obtained from Combi-Blocks (USA). 5,5′-dithiobis (2-nitrobenzoic acid) (DTNB, 99 %) was purchased from Fluorochem (UK). 3,3′,5,5′-Tetramethylbenzidine (TMB, 99 %) was purchased from Acros Organics (USA). Fetal bovine serum (FBS) was purchased from Hyclone (USA). HA (Mw 30 k–50 k Da) was obtained from Glentham Life Science (UK). Hoechst 33342 was purchased from Invitrogen. The JC-1 assay kit was purchased from MedChemExpress (USA). Calcein-AM was obtained from AAT Bioquest (USA). BODIPY TM 581/591 C11 was obtained from Thermo Fisher Scientific (USA). Anti-Ki67 antibodies (no ab15580) and anti-glutathione peroxidase 4 (GPX4) antibodies (no ab125066) were purchased from Abcam. All other chemicals were reagent grade and used as received. CT26 cells (murine colon cancer cell line), PC9 cells (human non-small cell lung cancer cell line), and WS1 cells (human skin fibroblast cells) were acquired from the Food Industry Research and Development Institute (Hsinchu City, Taiwan).

2.2. Synthesis and characterization of HA-SH adducts

The HA-SH adducts employed in this study were attained through the EDC/NHS-mediated amidation of cysteamine molecules and HA segments [38]. The detailed synthetic pathway of HA-SH is revealed in Scheme S1. First, HA (68.1 mg), NHS (41.4 mg), and EDC (103.5 mg) were dissolved in deionized water (3.0 mL) and stirred at room temperature for 2 h to activate the carboxylic group of HA. Afterward, cysteamine (60 mg) in deionized water (0.45 mL) was added to the above solution, followed by 1.0 N NaOH to adjust the pH to 6.0. The solution was stirred at room temperature for 24 h, followed by dialysis (Biomate MWCO 12000–14,000) against 0.1 M NaCl solution (pH 3.5) for 48 h and deionized water for 24 h. After being collected by lyophilization, the HA-SH adducts were characterized by ^{1}H NMR (Agilent DD2 600 MHz NMR spectrometer) and FT-IR (FT-720 spectroscopy, HORIBA, Japan).

2.3. Preparation of HA-decorated PDA (HP) nanoparticles

Based on a previously reported approach [35], the PDA nanoparticles utilized in this work were prepared by the oxidative self-polymerization of DA. Briefly, 35.8 mg DA·HCl was dissolved in 20 mL deionized water and stirred at 50 °C for 30 min. Subsequently, 150 μL of NaOH solution (1 N) was added to the above solution and gently stirred at 50 °C for 5 h. The solution was dialyzed (Biomate MWCO 6000–8000) with 0.01 M phosphate buffer (pH 8.0) at 4 °C to remove unreacted DA. To obtain the HP nanoparticles, 37.5 μL of HA-SH dissolved in pH 8.0 phosphate buffer (10 mg/mL) was added to 1.29 mL aqueous solution of PDA nanoparticles (1.75 mg/mL), and the mixing solution was stirred at room temperature for 24 h. Afterward, the HP nanoparticle-containing solution was dialyzed (Biomate MWCO 12000–14,000) against pH 8.0 phosphate buffer and stored at 4 °C for subsequent use. For comparison, the HP nanoparticles with different HA coating contents were prepared by changing the weight ratio of HA-SH and PDA in the feed.

2.4. Preparation of HCIP nanozymes

To prepare the HCIP nanozymes, 15 μL of $CuCl_2 \cdot 2H_2O$ aqueous solution (30 mg/mL) was added dropwise into 1.29 mL of PDA nanoparticle solution (1.75 mg/mL), and the mixture was stirred at 25 °C for 1.5 h. Subsequently, 75 μL of IR820 solution (4 mg/mL) was added dropwise into the above solution and stirred in the dark for 30 min, followed by the addition of HA-SH solution (10 mg/mL, 37.5 μL) and stirring for 24 h. Next, the resulting solution was dialyzed (Biomate MWCO 12000–14,000) against pH 8.0 phosphate buffer at 4 °C to remove unloaded Cu^{2+} and IR820. For comparison, HA-Cu^{2+}@PDA (HCP) nanozymes and HA-IR820@PDA (HIP) nanoparticles were prepared in a similar approach.

2.5. Characterization

The absorption spectra of DA monomers, IR820 molecules, PDA and HP nanoparticles, and HCIP nanozymes dispersed in pH 7.4 phosphate buffer were attained with a UV/Vis spectrophotometer (V-730, JASCO, Japan). The FT-IR spectra of PDA and HP nanoparticles were obtained using a FT-IR (FT-720 spectroscopy, HORIBA, Japan). The particle size and size distribution of PDA-based nanoparticles and nanozymes in aqueous solutions of different pH were measured with a Brookhaven BI-200SM goniometer equipped with a solid-state laser (35 mW, $\lambda = 637$ nm), and their zeta potential was determined by a Litesizer 500 (Anton Paar, USA). Each sample was measured at least three times, and the results were averaged. Furthermore, the angle-dependent autocorrelation functions and the ratio of the root-mean-square radius of gyration (R_g) to the mean hydrodynamic radius (R_h) of HCIP nanozymes in pH 7.4 0.15 M phosphate-buffered saline (PBS) were obtained by dynamic and static light scattering (DLS/SLS) measurements using the aforementioned BI-200SM goniometer. X-ray photoelectron spectroscopy (XPS) analysis was carried out using a PHI 5000 VersaProbe III X-ray photoelectron spectrometer (ULVAC-PHI, Japan). Thermogravimetric analysis (TGA) was performed by a thermogravimetric analyzer EXSTAR TG/DTA 6200 (Seiko Instruments Inc.) in an N_2 atmosphere. The sample was heated to 900 °C at 10 °C/min. The morphology of PDA-based nanoparticles and nanozymes was observed by scanning electron microscope (SEM) (JEOL JSM-7800F Prime Schottky Field Emission SEM, Japan) and transmission electron microscope (TEM) (JEM-1400, FLASH, JEOL, Japan). X-ray energy dispersive spectroscopy (EDS) elemental mapping of HCIP nanozymes was attained using TEM (JEM-F200, JEOL).

2.6. Determination of Cu^{2+} and IR820 content

To determine the Cu^{2+} content of PDA-based nanozymes, the nanozymes were diluted 20 times with HNO_3 solution (1 %) for complete Cu^{2+} dissociation. The Cu^{2+} concentration was quantified by inductively coupled plasma-atomic emission spectrometry (ICP-AES) with an Agilent 725 emission spectrometer.

To determine IR820 content, the HCIP nanozyme solution was

centrifuged, and the absorbance of the supernatant at 818 nm was measured using a UV/Vis spectrophotometer. The calibration curve utilized for drug loading characterization was attained by the absorbance of IR820 with different concentrations in a pH 8.0 phosphate buffer. The following formulas were used to calculate the IR820 loading efficiency (LE) and loading content (LC).

$$\text{LE}\ (\%) = \frac{amount\ of\ IR820\ in\ feed - amount\ of\ unloaded\ IR820}{Amount\ of\ IR820\ in\ feed} \times 100\%$$

$$\text{LC}\ (\%) = \frac{weight\ of\ loaded\ IR820}{Total\ weight\ of\ HCIP\ nanozymes} \times 100\%$$

2.7. In vitro Cu^{2+} and IR820 liberation

For the in vitro Cu^{2+} dissolution study, HCIP nanozyme solution (0.01 mL) was dispersed in pH 7.4 phosphate buffer and pH 5.0 acetate buffer (1.0 mL), respectively, and shaken at 100 rpm and 37 °C. The solution was taken out at the prescribed time, followed by centrifugation (16,000 rpm, 10 min) to acquire the supernatant. 0.25 mL of supernatant was mixed with 0.25 mL of vitamin C (40 mM) and 0.5 mL of BCS (2 mg/mL). After a 30-min reaction, the absorbance of the solution at 483 nm was examined with a UV/Vis spectrophotometer.

$$\text{Cumulative } Cu^{2+} \text{ release } (\%) = A_t/A_o \times 100\%$$

A_o = the absorbance of pristine HCIP nanozymes treated with vitamin C and BCS.

A_t = the absorbance of supernatant treated with vitamin C and BCS.

For the in vitro IR820 release test, the HCIP nanozyme solution (1.0 mL) was dialyzed (Biomate MWCO 12000–14,000) against pH 7.4 PBS and pH 5.0 acetate buffer (15 mL), respectively. The internal sample was periodically withdrawn at specified intervals to measure the maximum IR820 absorbance using the UV/Vis spectrophotometer (U2900, Hitachi, Japan). After each analysis, the sample was returned to the dialysis tube. The following formula was used to estimate the cumulative IR820 liberation (%).

$$\text{Cumulative IR820 liberation } (\%) = ((A_o - A_t)/A_o) \times 100\%$$

A_o = Initial IR820 absorbance.

A_t = IR820 absorbance at different time points.

2.8. Photothermal conversion performance

Free IR820, PDA, HP, and HIP nanoparticles, HCP, and HCIP nanozymes were dispersed in pH 7.4 PBS (1.0 mL), respectively, and exposed to irradiation of 808 nm NIR laser (1.0 W/cm^2) for 5 min. In this work, the PDA and IR820 concentrations were fixed at 0.2 mg/mL and 56.5 μM. During laser irradiation, the solution temperatures and thermal images were measured using an infrared thermal imaging camera (Thermo Shot F20, NEC Avio Infrared Technologies, Germany). Moreover, the temperature elevation of the aqueous solutions containing HCIP nanozymes of various concentrations exposed to laser irradiation (1.0 W/cm^2) or HCIP nanozymes (313 μg/mL) irradiated by 808 nm laser of different power densities was recorded by the above apparatus. On the other hand, the infrared thermal imaging camera was used to measure the temperature change of an aqueous solution of HCIP nanozymes (313 μg/mL) exposed to 808 nm laser irradiation for 5 min and cooled to room temperature. The photothermal conversion efficiency of HCIP nanozymes was estimated using the previously reported eq. [35]. For comparison, the photothermal conversion efficiency of free IR820 molecules, PDA, and HP nanoparticles was determined similarly. To assess the photothermal stability, the aqueous solutions of free IR820 molecules (56.5 μM), HP nanoparticles (270 μg/mL), and HCIP nanozymes (IR820 concentration = 56.5 μM) were subjected to irradiation of 808 nm laser (1.0 W/cm^2) with 5-min laser on and 5-min laser off for three cycles.

2.9. Catalytic activity

The catalytic activity (•OH production) of HCP nanozymes was assessed by the TMB assay. Through the •OH-induced TMB oxidation, the absorption of oxTMB at 665 nm can be enhanced. HCP nanozymes (334 μg) were dispersed in 4 mM H_2O_2 and 0.5 mM TMB-containing aqueous solutions of pH 7.4 and 5.0 (1.0 mL), then incubated in the dark at 37 °C for 10 min. After the solution was centrifuged at 16000 rpm for 10 min, the absorption of the collected supernatant was determined using a UV/Vis spectrophotometer. Moreover, to evaluate the effects of the reaction time on the •OH generation, the treatment time of HCP nanozymes with H_2O_2 and TMB was adjusted from 5 to 20 min, and the absorption of oxTMB was measured by the aforementioned approach. For exploring the effects of reaction temperature on the •OH production, the HCP nanozymes were treated with H_2O_2 and TMB at various solution temperatures for 10 min, and the absorption of oxTMB was measured by the aforementioned method. Similarly, the H_2O_2/TMB-treated HCP nanozymes were exposed to 10-min laser irradiation (1.0 W/cm^2), and the absorption of oxTMB was measured. On the other hand, the ABTS assay was employed to explore the •OH-producing performance of HCIP nanozymes. 0.167 mL of HCIP nanozymes (2.35 μg/mL) was added to aqueous solutions of pH 7.4 and 5.0 (0.833 mL) containing 100 μM H_2O_2 and 0.5 mM ABTS, and the solutions were incubated in the dark at 37 °C for 20 min. The solutions were centrifuged (16,000 rpm, 10 min), and the supernatant was collected for absorption analysis.

2.10. Photo-triggered $^1O_2$ production

DPBF as a $^1O_2$ probe was used to assess the NIR-triggered $^1O_2$ generation of IR820-containing formulations. The IR820 molecules, HIP nanoparticles, or HCIP nanozymes (IR820 concentration = 56 μg/mL) were dispersed in an aqueous solution of DPBF (0.24 mg/mL) and irradiated with NIR laser (808 nm, 1 W/cm^2) for 2.5, 5, and 10 min. Subsequently, the absorption of DPBF in the range 300–600 nm was measured using a UV/Vis spectrophotometer (U2900, Hitachi, Japan).

2.11. Cu^{2+}-mediated GSH depletion capability

The GSH-consuming activity of various PDA-based formulations was evaluated using the DTNB assay. PDA nanoparticles, HP nanoparticles, HCP nanozymes, and HCIP nanozymes were dispersed in 1 mL of an aqueous solution containing 0.1 mM GSH, respectively, and incubated at 37 °C for 2, 4, and 8 h. Afterwards, the mixture was centrifuged (16,000 rpm, 10 min), and the supernatant was mixed with 0.1 mL of DTNB (1 mM) for 15 min, followed by determination of TNB absorption in 300–600 nm. On the other hand, the BCS, as a Cu^+ chelator assay, was employed to verify that the HCIP nanozymes can deplete GSH by Cu^{2+}/Cu^+-mediated redox reaction. $CuCl_2$ molecules or HCIP nanozymes (Cu^{2+} concentration = 0.01 mg/mL) were reacted with GSH (0.4 mM) and BCS (0.1 mg/mL) at 37 °C for 1 h. The solution was centrifuged (16,000 rpm, 10 min), and the absorption of the supernatant in 400–600 nm was analyzed by a UV/Vis spectrophotometer. HP nanoparticles were also used as the control for comparison.

2.12. In vitro cellular uptake, intracellular cu^+ generation, and GSH consumption

The cellular internalization of HCIP nanozymes was explored using

CD44-overexpressing CT26 cells as a cell model. CT26 cells (2×10^5 cells/well) attached onto 22 mm round glass coverslips in 6-well plates were incubated with HCIP nanozymes (IR820 concentration: 7 μM) in the presence of HA segments (10 mg/mL) or not at 37 °C for 1 and 3 h. Free IR820-treated cells were used as a control group. The treated cells were washed twice with Hank's balanced salt solution (HBSS), followed by immobilization using 4 % formaldehyde and staining with Hoechst 33342. The cellular images were acquired by a CLSM (Olympus, FluoView FV3000, Japan) at 405 and 640 nm excitation wavelengths for Hoechst and IR820, respectively. Also, the effect of free HA addition on the cellular uptake of HCIP nanozymes by CT26 cells was assessed by FACSCalibur flow cytometer (BD Bioscience). After being treated with HCIP nanozymes (IR820 concentration: 7 μM) plus HA segments or not at 37 °C for 1 and 3 h, followed by detachment with trypsin-EDTA solution, the CT26 cells (2×10^5 cells/well) were suspended in PBS (1.0 mL), and the cellular IR820 fluorescence was analyzed by plotting fluorescence intensity on a log scale.

The coppersensor-1 was used to confirm the intracellular Cu^+ production from Cu^{2+}-rich nanozymes. CT26 cells were seeded onto 22 mm round glass coverslips in 6-well plates (2.0×10^5 cells/well), then incubated at 37 °C for 24 h. Afterward, the cells were exposed to IR820 (12 μg/mL), HP nanoparticles, HIP nanoparticles, HCP nanozymes, or HCIP nanozymes (HP concentration: 67.6 μg/mL) for 3 h. The treated cells were stained with coppersensor-1 (5 μM) at 37 °C for 30 min. The intracellular coppersensor-1 fluorescence was observed using fluorescence microscopy (ZEISS Axio Imager M2) at an excitation wavelength of 563 nm.

The intracellular GSH exhaustion of HCIP nanozymes was explored with the DTNB assay. After being seeded in a 6-well plate, CT26 cells (2×10^5/well) were incubated with HCIP nanozymes (Cu^{2+} concentration: 3 μg/mL, IR820 concentration: 12 μg/mL) for 24 h. The treated cells were washed twice with PBS, followed by detachment with trypsin-EDTA and centrifugation (1500 rpm) for 6 min. The obtained cell pellets were irradiated with 808 nm NIR laser (1.0 W/cm^2) for 5 min or not. The cells were then dispersed in RIPA lysis buffer and frozen overnight. The cells were then thawed for lysis and centrifuged (12,000 rpm, 10 min). The 0.1 mL of supernatant was mixed with 0.05 mL of 1 mM DTNB and analyzed by a microplate reader at a wavelength of 405 nm. For comparison, the intracellular GSH level of CT26 cells incubated with IR820, HP nanoparticles, HIP nanoparticles, and HCP nanozymes, respectively, was also assessed based on the above approach.

2.13. Intracellular ROS, mitochondrial damage, and LPO

The DCFH-DA was utilized to evaluate the intracellular ROS level. CT26 cells (2.0×10^5 cells/well) were seeded in 6-well plates containing 22 mm round glass coverslips and cultured for 24 h. Subsequently, the cells were incubated with IR820, HIP nanoparticles, or HCIP nanozymes (IR820 concentration: 12 μg/mL) for 3 h, and treated with or without 808 nm NIR laser irradiation (1.0 W/cm^2, 5 min). After adding HBSS containing DCFH-DA (5 μM) and 30 min incubation, the cells were imaged using fluorescence microscopy (ZEISS Axio Imager M2) at an excitation wavelength of 485 nm for DCF detection. For comparison, the intracellular ROS level of CT26 cells incubated with HP nanoparticles and HCP nanozymes (HP concentration: 67.6 μg/mL) with laser irradiation was also evaluated similarly.

To evaluate the mitochondrial damage induced by HCIP nanozymes, a JC-1 staining assay was used to detect the change in mitochondrial transmembrane potential. CT26 cells (2.0×10^5 cells/well) were seeded in 6-well plates with 22 mm round glass coverslips, followed by incubation at 37 °C for 24 h. Cells were cultured with IR820, HIP nanoparticles, or HCIP nanozymes (IR820 concentration: 12 μg/mL) for 3 h, and treated with or without 808 nm NIR laser irradiation (1.0 W/cm^2, 5 min). The cells were then treated with HBSS containing JC-1 (2 μg/mL) for 30 min and imaged using fluorescence microscopy (ZEISS Axio Imager M2) at 485 and 535 nm excitation wavelengths for JC-1 monomer and JC-1 aggregate, respectively. The mitochondrial transmembrane potential of CT26 cells incubated with HP nanoparticles and HCP nanozymes (HP concentration: 67.6 μg/mL) plus laser irradiation was also evaluated similarly for comparison.

The C11 BIDOPY$^{581/591}$ assay was employed to explore the intracellular LPO. CT26 cells attached onto 22 mm round glass coverslips in 6-well plates (1.0×10^5 cells/well) were treated with IR820, HIP nanoparticles, or HCIP nanozymes (IR820 concentration: 12 μg/mL) for 3 h, and treated with or without 808 nm NIR laser irradiation (1.0 W/cm^2, 5 min). The cells were then treated with HBSS containing C11 BIDOPY$^{581/591}$ (2 μM) for 30 min and imaged using fluorescence microscopy (ZEISS Axio Imager M2) at an excitation wavelength of 500 nm. The LPO of CT26 cells incubated with HP nanoparticles and HCP nanozymes (HP concentration: 67.6 μg/mL) plus laser irradiation was also evaluated similarly for comparison.

2.14. In vitro anticancer efficacy of combination therapy

CT26 cells (1.5×10^5 cells/well) in a 6-well plate were incubated with HP nanoparticles, HIP nanoparticles, HCP nanozymes, or HCIP nanozymes of different concentrations at 37 °C for 3 h. Subsequently, after being washed twice with PBS and detached with trypsin-EDTA, the cells were centrifuged (1500 rpm) and the cell pellets were irradiated with 808 nm NIR laser (1.0 W/cm^2) for 1 min. The treated cells were reseeded in a 12-well plate and incubated for 24 h. MTT (0.25 mg/mL, 1.0 mL) was added to each well, and the plates were incubated at 37 °C for 3 h. After removing the culture medium, DMSO (0.8 mL) was added to dissolve the formed precipitate. The absorbance of the resulting solution was then measured at 570 nm using a BioTek 800TS microplate reader. For comparison, the viability of CT26 cells treated with the above formulations without NIR laser irradiation was also evaluated using a similar approach. Moreover, the cytotoxicity of HCIP nanozymes against PC9 cells, a human non-small cell lung cancer, was assessed using the same approach with laser irradiation. On the other hand, the cytotoxicity of HCIP nanozymes on healthy WS1 cells, human skin fibroblast cells, was evaluated. WS1 cells (1×10^4 cells/well) in a 96-well plate were incubated with HCIP nanozymes of different concentrations at 37 °C for 3 h. After removing the culture medium and adding fresh medium, the cells were incubated for 24 h. Afterwards, the MTT assay described above was used to determine the cell viability.

The live and dead cells were stained with calcein-AM and PI to further confirm the cytotoxicity of various formulations on CT26 cells. CT26 cells (2×10^5 cells/well) in a 12-well plate were incubated with HP nanoparticles, HIP nanoparticles, HCP nanozymes, and HCIP nanozymes (HP concentration: 67.6 μg/mL), respectively, for 3 h. Afterwards, cells were irradiated using 808 nm NIR laser (1.0 W/cm^2) for 1 min, followed by staining with calcein-AM (2 μg/mL) for 45 min and PI (4 μg/mL) for 15 min. The treated cells were observed by a NIB-100F inverted fluorescent biological microscope.

2.15. In vitro hemolysis assay

0.5 mL of erythrocyte suspension (0.2 %, *v*/v) was mixed with 0.5 mL of HP nanoparticles and HCIP nanozyme and incubated at 37 °C for 0.5 h, respectively. The erythrocytes incubated in deionized water and 0.9 % saline solution were used as the positive and negative controls, respectively. After centrifugation at 16000 rpm for 10 min, the optical density (OD) of each solution was measured at 540 nm using a UV/Vis

spectrophotometer (U2900, Hitachi, Japan). The hemolysis rate was calculated as follows:

$$\text{hemolysis rate}\ (\%) = \left(\frac{OD\ value\ of\ experimental\ group - OD\ value\ of\ saline\ group}{OD\ value\ of\ deionized\ water\ group - OD\ value\ of\ saline\ group}\right) \times 100\%.$$

2.16. Animals and tumor model

Female BALB/c mice (5–6 weeks old) were acquired from the National Laboratory Animal Center (Taiwan). The animal studies (IACUC Approval No: 112040) adhere to the guidelines approved by the Administrative Committee on Animal Research at Chung Shan Medical University (Taiwan). To obtain the tumor model, 5×10^6 CT26 cells in 0.1 mL PBS were injected subcutaneously into the right thigh of the mice. Tumor volume (V) was estimated as $V = L \times W^2/2$. W is the tumor measurement at the widest point, and L is the tumor dimension at the longest.

2.17. In vivo biodistribution

When tumor volume reached 80–120 mm^3, 100 μL of aqueous solutions containing free IR820 molecules or HCIP nanozymes were injected into the mice via the tail vein (IR820 dosage of 1.0 mg/kg). At 2, 4, 6, 24, and 48 h post-injection, the in vivo biodistribution of free IR820 molecules and HCIP nanozymes was monitored by fluorescence signals of IR820 (Ex. 710 nm and Em. 830 nm) using an IVIS imaging system (IVIS Lumina II, Caliper, LifeSciences, MA, USA). At 48 h post-injection, the treated mice were sacrificed by CO_2 euthanasia, followed by imaging of the collected major organs and tumors with IVIS imaging system.

2.18. In vivo tumor hyperthermia and growth inhibition

When the tumor volume of mice reached 80–120 mm^3, mice were randomly divided into seven groups ($n = 4$): (1) control; (2) HP nanoparticles; (3) HCIP nanozymes; (4) IR820 + NIR laser; (5) HCP nanozymes + NIR laser; (6) HIP nanoparticles + NIR laser, (7) HCIP nanozymes + NIR laser. Mice in different groups were intravenously injected with 100 μL of the corresponding reagents. The 1.0 mg/kg dosages for IR820 and 5.6 mg/kg for HP were used. Each group was subjected to two doses at days 0 and 2. At 4 h post-injection, the tumor sites of mice in corresponding groups were irradiated with 808 nm laser (1.0 W/cm^2) for 5 min. The tumor temperature was monitored during laser irradiation using an infrared thermal imaging camera. The tumor volumes and body weight of various groups were recorded every two days. At day 18 post-treatment, all mice were euthanized. The tumors and major organs (heart, liver, spleen, lung, kidney) were gathered, and the tumor and spleen were weighed. Afterwards, the tumors and organs were sectioned into 4 μm-thick slices for individual staining of hematoxylin and eosin (H&E), anti-Ki67 antibodies, and anti-GPX4 antibodies, and then observed by an Olympus IX70 inverted microscope (Japan).

2.19. Statistical analysis

Data are reported as mean ± SD. The differences among groups were determined using one-way or two-way ANOVA analysis; ns > 0.05, $^*p < 0.05$, $^{**}p < 0.01$, $^{***}p < 0.001$, $^{****}p < 0.0001$.

3. Results and discussion

3.1. Synthesis and characterization of HA-SH adducts

The HA-SH adducts utilized to decorate PDA nanoparticles

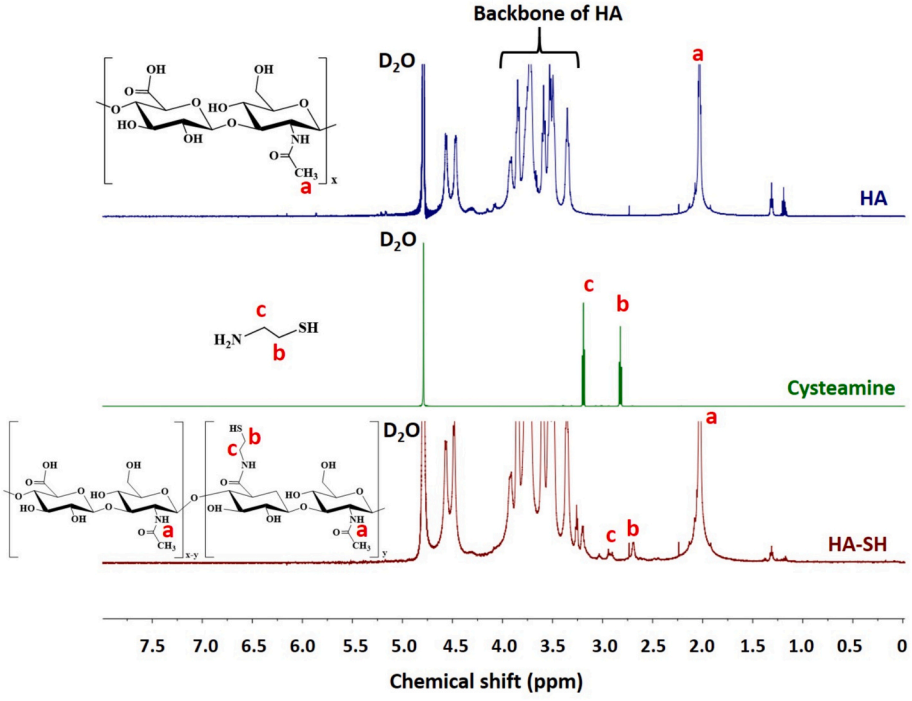

Fig. 1. ^1H NMR spectra of HA, cysteamine, and HA-SH in D_2O.

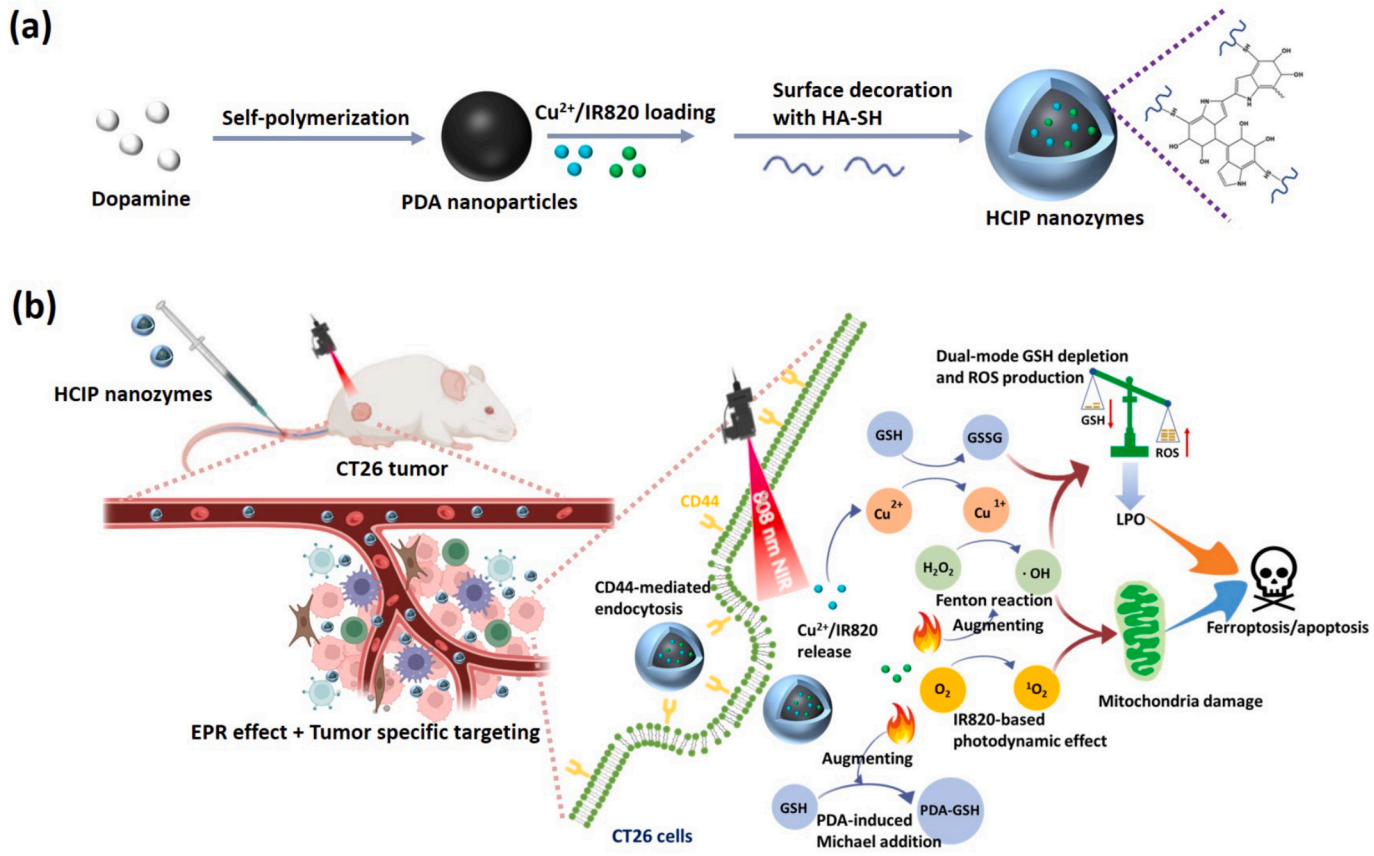

Scheme 1. Schematic design of (a) preparation of HCIP nanozymes and (b) their antitumor effect by photothermal-boosted catalytic therapy and PDT combined with ferroptosis.

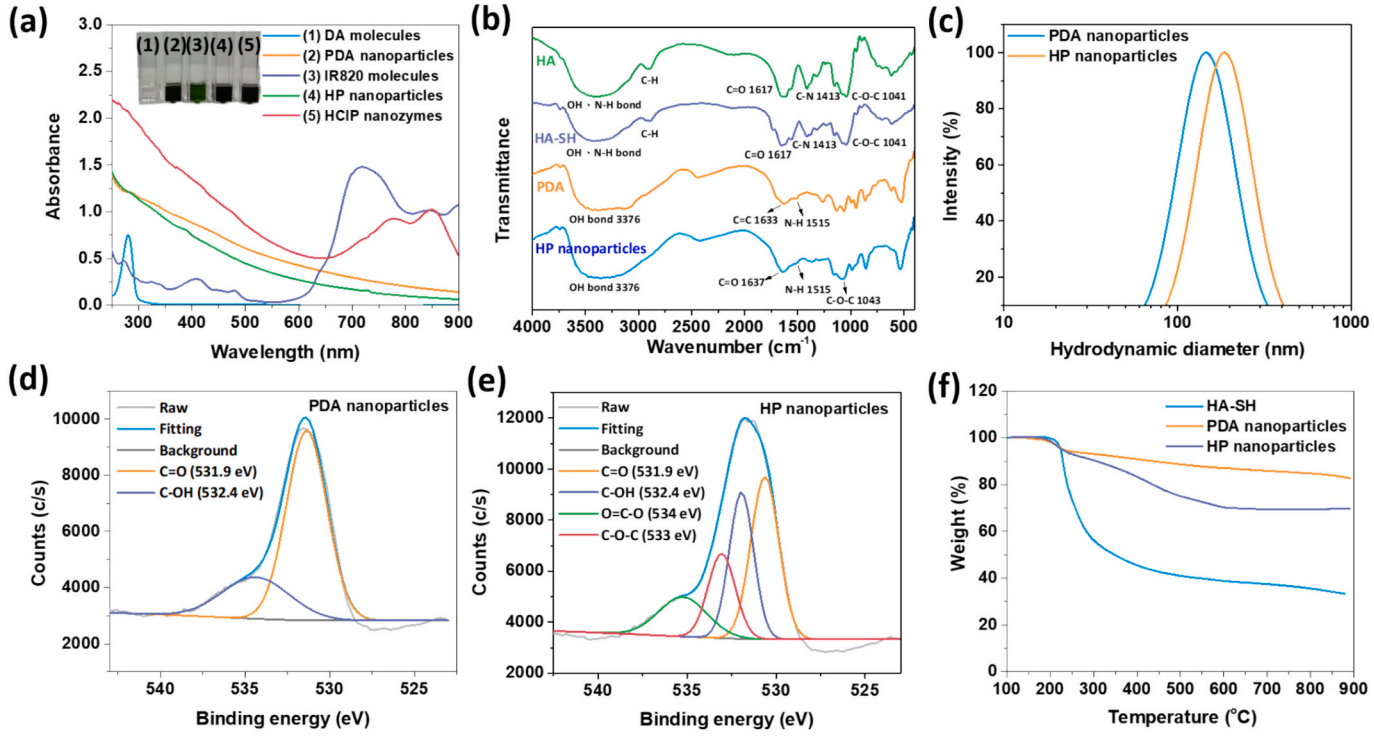

Fig. 2. (a) Absorption spectra and photos of aqueous solutions of DA monomers, PDA nanoparticles, IR820 molecules, HP nanoparticles, and HCIP nanozymes. (b) FT-IR spectra of HA, HA-SH, PDA, and HP nanoparticles. (c) Particle size distribution curves of PDA and HP nanoparticles dispersed in pH 7.4 aqueous solution (I = 0.01 M). O1s XPS spectra of (d) PDA and (e) HP nanoparticles. (f) TGA profiles of HA-SH segments, PDA nanoparticles, and HP nanoparticles.

Table 1
Particle size and Cu^{2+}/IR820 loading capability of various PDA-based formulations ($n = 3$).

Sample	D_h (nm)	PDI	Cu^{2+} loading content (wt%)	IR820 loading content (wt%)
PDA nanoparticles	138 ± 4	0.09 ± 0.04	–	–
HP nanoparticles	178 ± 10	0.13 ± 0.03	–	
HIP nanoparticles	186 ± 12	0.21 ± 0.04	–	13.2 ± 0.4
HCP nanozymes	179 ± 7	0.15 ± 0.05	4.9 ± 0.2	–
HCIP nanozymes	179 ± 8	0.18 ± 0.02	3.7 ± 0.2	14.9 ± 0.6

covalently were obtained by the DCC/NHS-mediated amidation reaction of cysteamine with carboxylic acid groups of HA segments [38], and characterized by ^{1}H NMR spectroscopy. As shown in the ^{1}H NMR spectrum of HA-SH adducts (Fig. 1), the presence of feature methylene proton signals of cysteamine at δ 2.7 ppm confirms the successful conjugation of cysteamine with HA. Moreover, according to the signal integral ratio of the methylene protons of cysteamine at δ 2.7 ppm and the acetyl methyl protons (δ 2.0 ppm) from HA, the degree of substitution of HA with cysteamine, defined here as the number of thiol groups per 100 β4-glucuronic acid-β3-*N*-acetylglucosamine units, was estimated to be ca 30.

3.2. Preparation and characterization of photothermal HCIP nanozymes

As presented in Scheme 1a, the PDA nanoparticles were attained upon the self-polymerization of DA molecules in NaOH solution at 50 °C. Notably, different from the DA solution with a nearly transparent state and a sharp absorption peak at 281 nm (Fig. 2a), the black PDA nanoparticle solution showed visibly augmented absorption from visible to NIR light. Similar UV/Vis spectra of PDA nanoparticles and DA molecules were reported elsewhere [31,39]. As shown in the FT-IR spectrum of PDA nanoparticles (Fig. 2b), two weak feature bands of indole and indoline at 1633 and 1515 cm^{-1}, respectively, were observed. These results confirm the effective oxidative polymerization of DA monomers into PDA nanoparticles. The hydrodynamic diameter of PDA nanoparticles dispersed in pH 7.4 phosphate buffer ($I = 0.01$ M) was determined to be ca 138 ± 4 nm (Table 1 and Fig. 2c). Notably, after being transferred from phosphate buffer to PBS (pH 7.4, $I = 0.15$ M) for 1 h, the PDA nanoparticles displayed an enlarged particle size from 138 ± 4 nm to 336 ± 26 nm (Fig. S1). With the time being prolonged from 1 h to 24 h, the particle size of PDA nanoparticles further increased beyond 1000 nm (Fig. S1), indicating serious aggregation of PDA nanoparticles. Some studies also reported the salting-out-elicited aggregation of PDA nanoparticles under physiological salt conditions [40,41]. To endow PDA nanoparticles with robust colloidal stability and active CD44 receptor-targeting capability for tumor-targeted delivery of Cu^{2+} and IR820, the as-synthesized HA-SH adducts were covalently conjugated on the surfaces of PDA nanoparticles (HA-SH/PDA feeding weight ratio = 0.17) upon the Michael addition between thiol groups of HA-SH segments and quinone residues of PDA nanoparticles. As revealed in the XPS spectra (Fig. 2d and e), in addition to the feature peaks of C═O (531.9 eV) and C—O (532.4 eV) of PDA nanoparticles, two new peaks of C-O-C (533 eV) and O=C-O (534 eV) from HA-SH segments were observed for HP nanoparticles. Also, the absorption band of C-O-C stretching vibration from HA-SH segments at 1043 cm^{-1} was observed in the UV/Vis spectrum of HP nanoparticles (Fig. 2b). The findings demonstrate the successful coupling of HA-SH adducts with PDA nanoparticles. Note that after being conjugated with HA-SH adducts, the PDA nanoparticles showed increased particle size from 138 ± 4 to 178 ± 10 nm in pH 7.4 aqueous solution ($I = 0.01$ M) due to the presence of HA-rich coating layers (Table 1, Fig. 2c). Based on the TGA profiles in Fig. 2f, the HP nanoparticles were composed of ca 74 wt% PDA and 26 wt% HA. Notably, the HP nanoparticles maintained nearly unchanged particle size in pH 7.4 0.15 M PBS during 24 h (Fig. S2), distinct from the salt-elicited massive aggregation of PDA nanoparticles in the same environment. This indicates that the hydrophilic HA surface coating

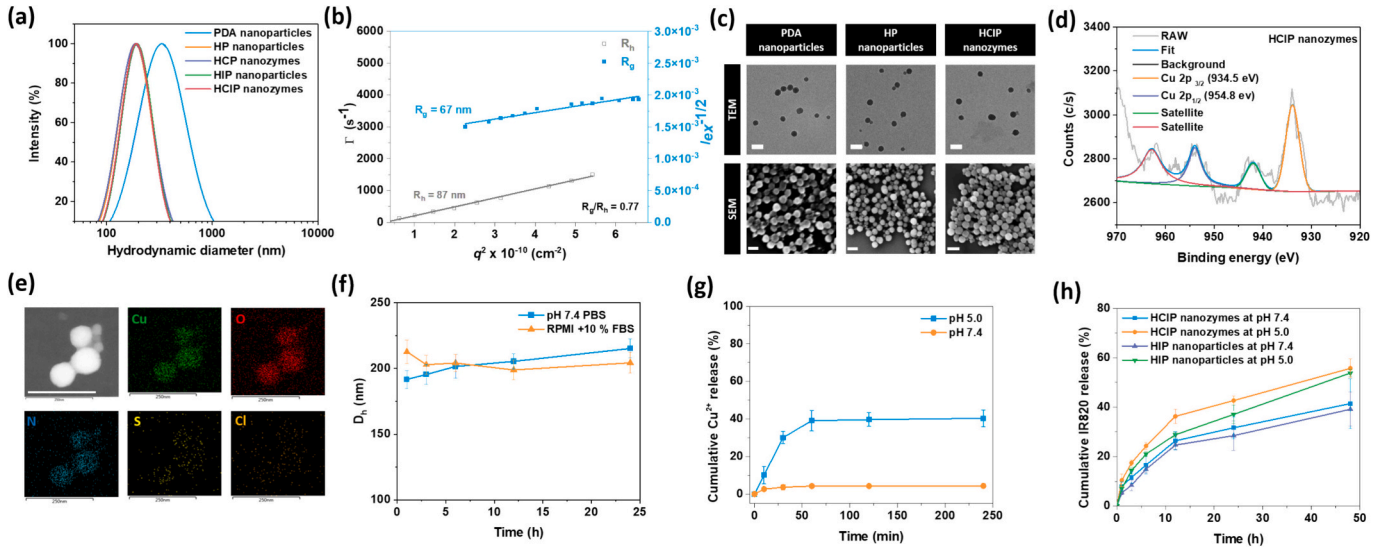

Fig. 3. (a) Particle size distribution curves of PDA nanoparticles, HP nanoparticles, HCP nanozymes, HIP nanoparticles, and HCIP nanozymes dispersed in pH 7.4 0.15 M PBS for 1 h. (b) Angle-dependent DLS and SLS measurements of HCIP nanozymes in pH 7.4 0.15 M PBS. (c) TEM and SEM images of PDA nanoparticles, HP nanoparticles, and HCIP nanozymes. (d) Cu 2p spectrum of HCIP nanozymes. (e) Elemental mapping images of HCIP nanozymes. Scale bar: 250 nm. (f) Colloidal stability of HCIP nanozymes dispersed in pH 7.4 PBS and 10 % FBS-containing RPMI medium, respectively, at 37 °C ($n = 3$). (g) Cumulative Cu^{2+} release profiles of HCIP nanozymes at pH 5.0 and 7.4 at 37 °C (n = 3). (h) Cumulative IR820 liberation profiles of HCIP nanozymes and HIP nanoparticles at pH 5.0 and 7.4 at 37 °C (n = 3).

could enhance the colloidal stability of HP nanoparticles under physiological salt conditions, which is a key prerequisite for extended blood circulation of nanoparticles. Furthermore, when the HA-SH/PDA feeding weight ratio was adjusted from 0.17 to 0.03, the particle size of HP nanoparticles dispersed in 0.15 M PBS was gradually enlarged over time (Fig. S3), signifying the occurrence of some particle aggregation. This further verifies that a sufficient amount of HA decorated on the PDA nanoparticles is very important to promote the colloidal dispersion of HP nanoparticles. Due to the outstanding colloidal stability, the HP nanoparticles with a fixed HA-SH/PDA feeding weight ratio of 0.17 were employed as vehicles for Cu^{2+} and IR820 delivery.

Next, through the coordination of Cu^{2+} with catechol groups of HP nanoparticles as well as the π-π stacking and hydrophobic interactions of IR820 with the HP nanoparticles, the HCIP nanozymes were obtained. Notably, the HCIP nanozymes exhibited a visible red shift of IR820 maximum absorption (Fig. 2a) due to the strong π-π stacking and hydrophobic interactions between IR820 and PDA. Such a red shift in the absorption of IR820 incorporated with PDA-containing nanoparticles was also reported elsewhere [39]. As presented in Table 1 and Fig. 3a, the particle size (ca 179 ± 8 nm) of HCIP nanozymes in 0.15 M PBS is comparable to that of HP nanoparticles. The angle-dependent DLS data of HCIP nanozymes showed a high linear correlation between the relaxation frequency (Γ) and the square of the scattering vector (q^2) (Fig. 3b), suggesting their nearly spherical shape. According to the Berry plot of the scattering intensity ($I_{ex}^{1/2}$) versus the square of the scattering vector (q^2) from angle-dependent SLS examination (Fig. 3b), the R_g value (ca 67 nm) of HCIP nanozymes was gained, and the estimated R_g/R_h ratio (ca 0.77) is close to that (0.78) of solid sphere-like polymeric nanoparticles as obtained elsewhere [42,43]. Also, the TEM and SEM images illustrated the uniform spherical form of HP nanoparticles and HCIP nanozymes (Fig. 3c). The high-resolution Cu 2p spectrum of HCIP nanozymes exhibited two characteristic peaks at 934.5 eV (Cu $2p_{3/2}$) and 954.8 eV (Cu $2p_{1/2}$) accompanied with two shake-up satellite peaks (Fig. 3d). Note that the presence of Cu, O, N, S and Cl elements was further visualized by the EDS mapping of HCIP nanozymes (Fig. 3e). These findings demonstrate that the HCIP nanozymes have a spherical architecture comprising a PDA core loaded with Cu^{2+} and sulfonate-containing IR820, and hydrophilic HA-rich surface (Scheme 1a). In addition, the Cu^{2+} loading content in HCIP and HCP nanozymes was determined by ICP-AES analysis to be ca 3.7 ± 0.2 and 4.9 ± 0.2 wt% (Table 1). The IR820 loading contents of HCIP nanozymes and HIP nanoparticles were measured to be ca 14.9 ± 0.6 and 13.2 ± 0.4 wt%, respectively (Table 1). These results suggest that the HCIP nanozymes display satisfactory Cu^{2+} and IR820 loading capability. It should be highlighted that the HCIP nanozymes exhibited prominent colloidal stability as evidenced by virtually unvaried particle size in pH 7.4 PBS or 10 % FBS-containing RPMI during 24 h (Fig. 3f).

Although Cu^{2+} is a key metal element for CDT-mediated cancer treatment, excessive Cu^{2+} exposure in free form can be highly toxic and provoke many diseases [44,45]. Therefore, it is essential to preliminarily evaluate the in vitro release of Cu^{2+} from HCIP nanozymes at pH 7.4 (mimicking normal physiological conditions) and 5.0 (imitating intracellular acidic organelles). As revealed in Fig. 3g, the cumulative Cu^{2+} liberation of HCIP nanozymes was remarkably increased from 5 % to 40 % in response to a pH change from 7.4 to 5.0 during 24 h. Also, the negative zeta potential of PDA-containing nanoparticles and nanozymes was converted to approach a neutral value by reducing pH from 7.4 to 5.0 due to the increased protonation of phenolic hydroxyl groups (e.g., catechol residues) from PDA (Fig. S4). These results indicate that the acidity-activated protonation of catechol groups could diminish the coordination interaction between PDA and Cu^{2+} within HCIP nanozymes, thus accelerating Cu^{2+} outflow. Similar acidity-triggered Cu^{2+} liberation from PDA-rich nanoparticles was observed in other studies [45–47]. Furthermore, the promoted protonation of amine from

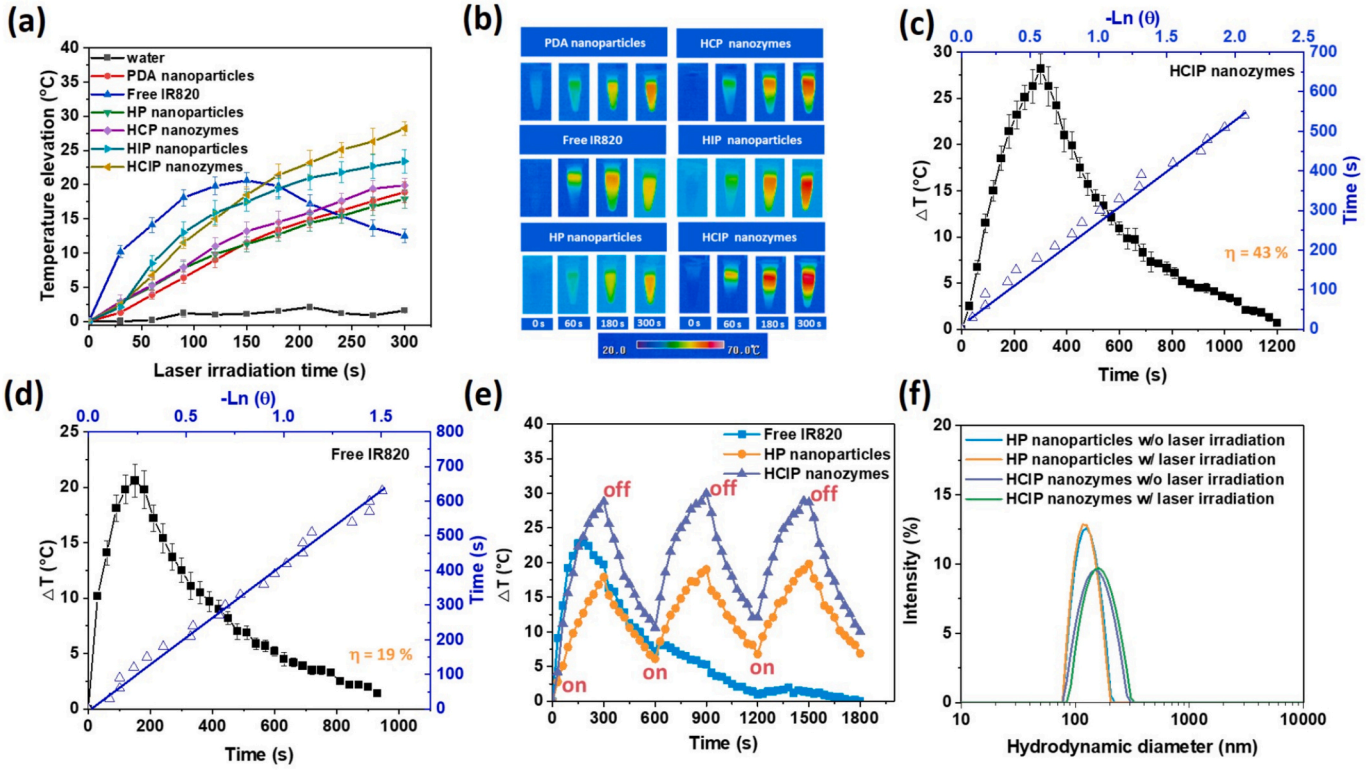

Fig. 4. (a) Temperature elevation curves and (b) thermal images of different formulations ($n = 3$). Photothermal effect and plot fitting of cooling time versus the negative natural logarithm of the driving force temperature during the cooling procedure of (c) HCIP nanozyme and (d) free IR820 solution (IR820 concentration: 56.5 μM) (n = 3). (e) Photothermal capability evaluation for aqueous solutions containing IR820 molecules, HP nanoparticles, or HCIP nanozymes receiving repeated NIR laser irradiation (808 nm, 1.0 W/cm^2). (f) Particle size distribution curves of HP nanoparticles and HCIP nanozymes with or without laser irradiation.

quinone or indoline groups in a weakly acidic environment partially declines the hydrophobic interaction of PDA with IR820, thus appreciably increasing IR820 liberation from HIP nanoparticles and HCIP nanozymes (Fig. 3h). Based on these findings, it was assumed that Cu^{2+} and IR820 of HCIP nanozymes could be efficiently released under acidic organelles such as endosomes and lysosomes (pH 4.5–6.0), whereas the premature leakage could be decreased under normal physiological conditions (pH 7.4), which is a boon for tumor-specific combined therapy. Also, the significantly reduced Cu^{2+} leakage from HCIP nanozymes at pH 7.4 was anticipated to minimize Cu^{2+}-related systemic toxicity. Given the short lifetime and limited diffusion distance of $^1O_2$, the acid-triggered IR820 release is advantageous, allowing the generated $^1O_2$ via remotely controlled laser irradiation to act on organelles without delay.

3.3. Photothermal effect and stability of HCIP nanozymes

Considering that the PDA nanoparticles and IR820 molecules can convert NIR light into heat, the NIR-trigged photothermal effect of HCIP nanozymes was evaluated by monitoring their solution temperature variation using an infrared thermal imaging camera. As presented in Fig. 4a and b, at the same PDA concentration (200 μg/mL), the aqueous solutions containing HCP nanozymes, PDA, or HP nanoparticles under NIR laser irradiation for 300 s showed comparable temperature elevation, indicating that the photothermal conversion capability of PDA nanoparticles was not affected by Cu^{2+} coordination and HA surface coating. Notably, compared to the aforementioned formulations, the HCIP nanozymes showed prominently amplified solution temperature elevation during the NIR laser irradiation, suggesting the enhanced photothermal effect of HCIP nanozymes by incorporating IR820 into HCIP nanozymes. Also, according to the photothermal heating-cooling curves (Fig. 4c), the photothermal conversion efficiency (η) of HCIP nanozymes was determined to be ca 43 %, being somewhat higher than that of PDA and HP nanoparticles (Fig. S5). On the other hand, due to photobleaching and thermal degradation of IR820 [39,48], free IR820 molecules had a poor photothermal conversion efficiency of ca 19 % (Fig. 4d), and the temperature rise of free IR820-containing solution declined gradually 150 s after irradiation (Fig. 4a and b). Importantly, after three on/off cycles of NIR laser irradiation, the HCIP nanozymes maintained nearly intact photothermal ability and particle size (Fig. 4e and f). In contrast, free IR820 molecules showed a vastly diminished photothermal effect due to serious photobleaching (Fig. 4e). As expected, the NIR-elicited temperature elevation of HCIP nanozyme solution was boosted by increasing the concentration of HCIP nanozymes (Fig. S6a). Also, the temperature elevation level of the HCIP nanozyme solution can be adjusted by changing the laser power density (Fig. S6b). This controllable photothermal effect of HCIP nanozymes could be beneficial for optimizing the application of clinical PTT. Based on these findings, compared to the free IR820 molecules, the designed HCIP nanozymes exhibited sound photothermal conversion capability, highly stable photothermal effect and stability, and good colloidal dispersion, thus being utilized as potential regents to enhance the anticancer efficacy of multiple therapies.

3.4. ·OH and $^1O_2$ production and GSH depletion

The ·OH production performance of Cu^{2+}-carrying nanozymes upon Fenton-like reaction was assessed using TMB as an indicator, which can be oxidized by ·OH to form the product with absorption at 650 nm. Notably, no significant absorption of TMB was observed in aqueous solutions containing H_2O_2 and HCP nanozymes at pH 7.4 (Fig. 5a). By contrast, the TMB in a pH 5.0 aqueous solution containing HCP nanozymes and H_2O_2 showed prominent absorption at 650 nm. Moreover, the absorbance of TMB in the HCP nanozyme/H_2O_2-containing solution at pH 5.0 was consistently enhanced by prolonging the reaction time from 5 to 20 min (Fig. 5b). This finding indicates that the HCP nanozymes could efficiently convert H_2O_2 into·OH in the weakly acidic environment upon Cu^{2+}-mediated Fenton-like reaction. Furthermore, the ·OH-producing capability of HCIP nanozymes in the H_2O_2-containing solution was evaluated by employing ABTS. With the pH of the HCIP nanozyme solution being adjusted from pH 7.4 to 5.0, the absorption of ABTS from visible light to NIR light was remarkably increased due to the increased oxidation of ABTS by·OH (Fig. 5c). These results suggest that the HCP and HCIP nanozymes under weakly acidic conditions could accelerate the Cu^{2+}-mediated Fenton-like reaction rate, thus promoting the conversion of H_2O_2 into ·OH. Some Cu^{2+}-containing nanoparticles also showed the acidity-activated Fenton-like reaction as reported elsewhere [27,30,49,50]. Because of the temperature dependence of the Fenton and Fenton-like reaction rate, as mentioned in the previous studies [36,37,45,51], the ·OH generation of HCP nanozymes at different temperatures was further assessed. As presented in Fig. 5d, the absorbance of TMB in a pH 5.0 aqueous solution containing HCP nanozymes and H_2O_2 was increased with the solution temperature being elevated from 4 to 37 °C, illustrating the promoted ·OH production upon thermal-enhanced Fenton-like reaction. Importantly, under NIR laser irradiation, the absorbance of TMB in the above solution was further increased, signifying that the PDA-mediated photothermal effect effectively augmented the Fenton-like reaction to amplify ·OH generation. Next, the photo-triggered $^1O_2$-generating capability of HCIP nanozymes was explored by DPBF, a $^1O_2$ indicator that displayed the declined absorbance at about 450–500 nm after being degraded by $^1O_2$. With irradiation of 808 nm NIR laser, different from nearly unchanged absorbance of DPBF molecules in HCP nanozyme solution (Fig. S7a), the absorbance of DPBF molecules in aqueous solutions containing HCIP nanozymes, HIP nanoparticles, or free IR820 molecules (IR820 concentration = 56 μg/mL) was remarkably decreased with the prolonged irradiation time (Fig. 5e, S7b and S7c), demonstrating $^1O_2$ production upon IR820-mediated photodynamic effect. Also, as revealed in Fig. 5f, during NIR laser irradiation, the normalized absorbance of DPBF molecules treated with HCIP or HIP nanozymes was appreciably declined relative to that of DPBF incubated with free IR820 molecules. Compared to IR820, the HCIP and HIP nanozymes exhibited superior $^1O_2$-generating performance, indicating that these nanozymes could mitigate the photo-bleaching effect of IR820, thereby enhancing the IR820-based photodynamic effect.

Increasing studies report that the high concentration of GSH in the tumor microenvironment largely restricts the anticancer efficacy of ROS-mediated therapy [16–18]. The DTNB, being reduced by GSH to form a yellow product with a characteristic absorption at 412 nm, was employed as an indicator to evaluate the GSH-depleting capability of HCIP nanozymes. Notably, the absorbance of DTNB in GSH solution pretreated with the PDA or HP nanoparticles for 8 h was appreciably lower than that of DTNB in GSH alone solution as the control group (Fig. 5g), indicating the GSH consumption by PDA-mediated Michael addition. Furthermore, at the same reaction time, the absorbance of DTNB in the GSH solution treated with HCP or HCIP nanozymes further decreased. This suggests that the HCP and HCIP nanozymes exhibited prominent GSH-depleting capability compared to PDA and HP nanoparticles. Moreover, the HCP and HCIP nanozymes showed faster GSH-consuming performance relative to PDA and HP nanoparticles (Fig. 5h). On the other hand, as shown in Fig. 5i, in the presence of GSH, distinct from no significant absorption of BCS molecules in the HP nanoparticle solution, the prominent absorption of BCS molecules (483 nm) in the aqueous solutions containing HCP or HCIP nanozymes was observed. This is because the Cu^{2+} ions released from HCP and HCIP nanozymes can be reduced by GSH to Cu^{+} ions that form yellow complexes with BCS. According to the above results, it can be concluded that the HCIP nanozymes can not only effectively deplete GSH by a combination of PDA with Cu^{2+} but also potently generate ·OH and $^1O_2$ under NIR irradiation, beneficial for achieving anticancer efficacy of the PTT integrated with ROS-based CDT and PDT (Fig. 5j).

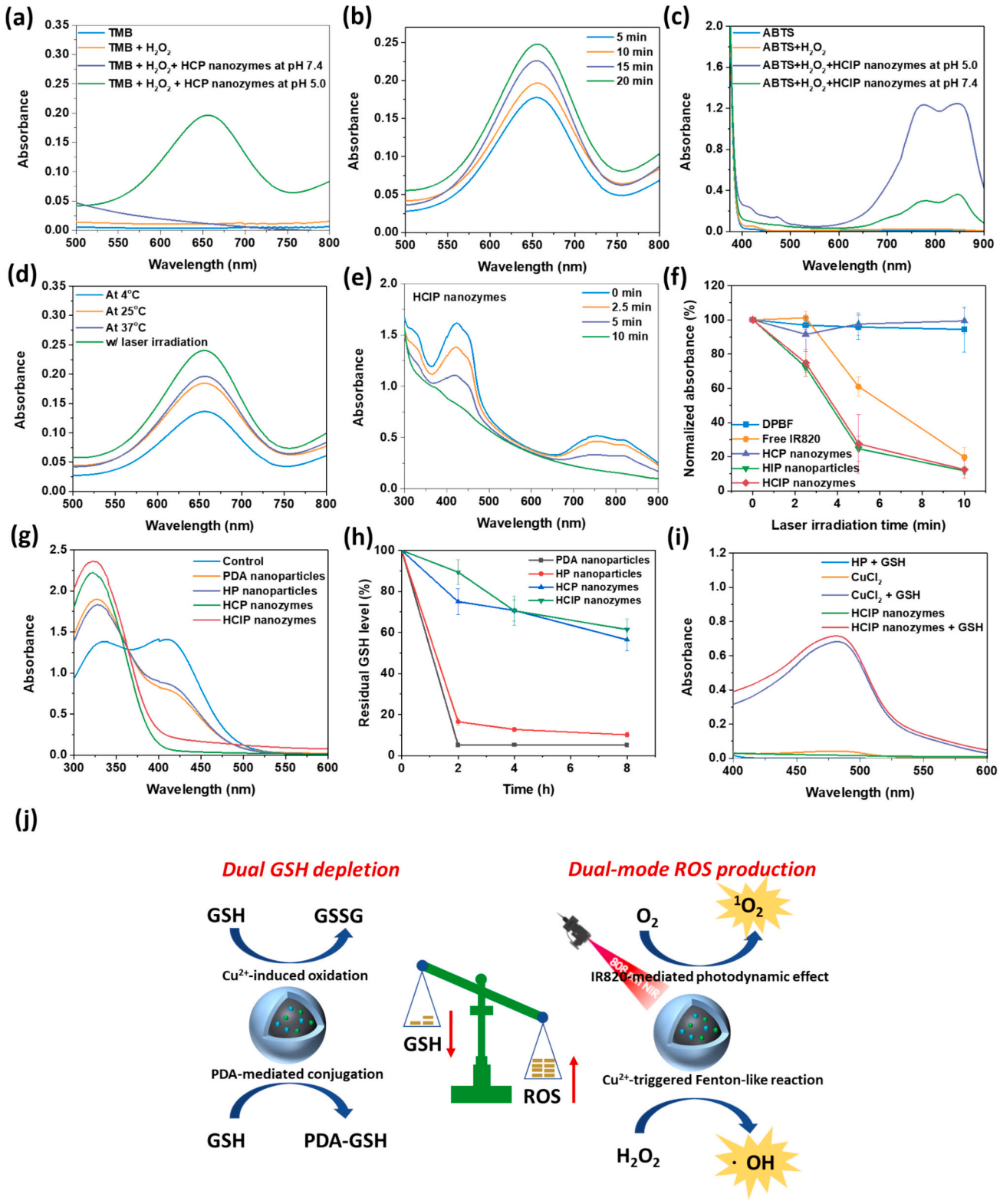

Fig. 5. (a) Absorption spectra of TMB molecules treated with HCP nanozymes/H_2O_2-containing solution at pH 7.4 or 5.0 and 37 °C for 10 min. (b) Absorption spectra of TMB molecules treated with HCP nanozymes/H_2O_2-containing solutions at pH 5.0 and 37 °C for various time intervals. (c) Absorption spectra of ABTS molecules treated with HCIP nanozymes/H_2O_2-containing solution at pH 7.4 or 5.0 and 37 °C for 20 min. (d) Absorption spectra of TMB molecules treated with HCP nanozymes/H_2O_2-containing solution at pH 5.0 and different temperatures or receiving laser irradiation (1 W/cm^2) for 10 min. (e) Absorption spectra of DPBF molecules in HCIP nanozyme solution exposed to laser irradiation for different times. (f) Normalized absorbance of DPBF molecules treated with various formulations and laser irradiation ($n = 3$). (g) Absorption spectra of DTNB molecules in the GSH solutions pretreated with different formulations for 8 h. (h) Residual level of GSH molecules treated with various formulations for different time intervals (n = 3). (i) Absorption spectra of BCS molecules receiving different formulation treatments. (j) Schematic illustration of dual-mode ROS production and GSH depletion of HCIP nanozymes.

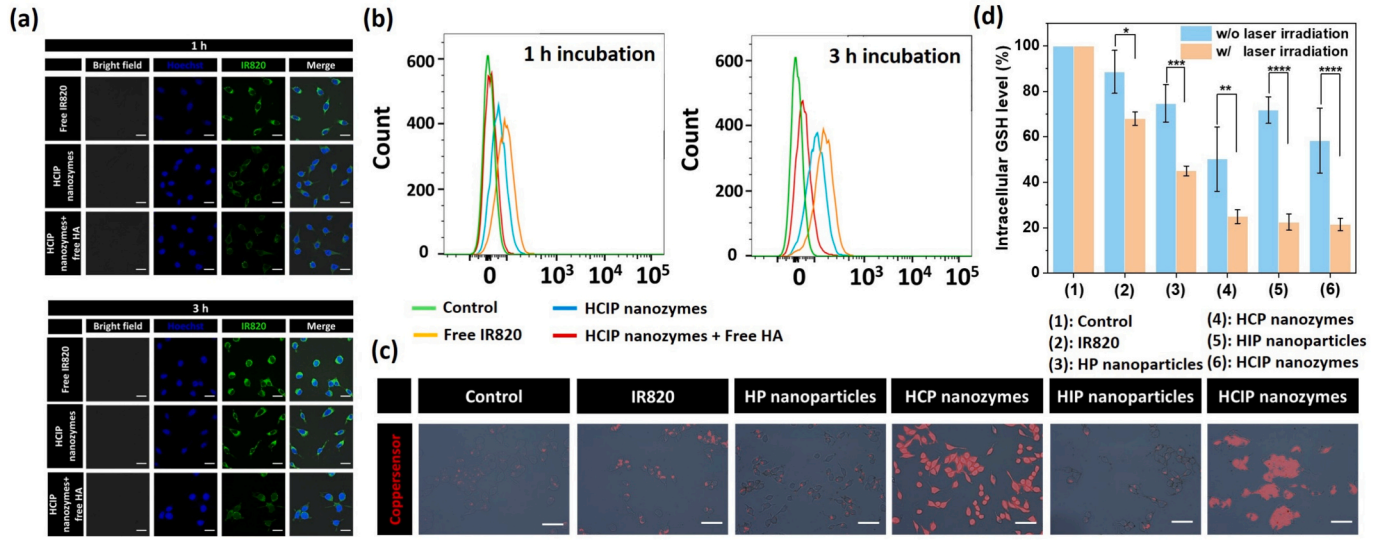

Fig. 6. (a) CLSM images and (b) flow cytometric profiles of CT26 cells incubated with IR820 molecules or HCIP nanozymes in the presence of free HA segments or not at 37 °C for 1 and 3 h. (c) Coppersensor staining of CT26 cells receiving different treatments. (d) Intracellular GSH levels of CT26 cells exposed to various formulations with or without laser irradiation ($n = 3$).

3.5. *In vitro cellular uptake, intracellular cu$^+$ production, and GSH depletion*

To explore the HA-mediated CD44-targeting capability of HCIP nanozymes, their internalization by CT26 colon cancer cells with CD44 overexpression was examined by CLSM and flow cytometry. As shown in the CLSM images (Fig. 6a), at 1-h or 3-h incubation, the intracellular IR820 fluorescence signals of CT26 cells treated with HCIP nanozymes were appreciably higher compared to those of CT26 cells incubated with both HCIP nanozymes and free HA molecules. With the incubation time being prolonged from 1 to 3 h, CT26 cells exposed to HCIP nanozymes showed remarkably enhanced intracellular IR820 fluorescence compared to cells treated with HCIP nanozymes plus free HA segments. Similar results were also obtained using flow cytometry (Fig. 6b). These findings strongly demonstrate that the HCIP nanozymes could be efficiently internalized by CT26 cells upon CD44-mediated endocytosis. In contrast, the cellular uptake of these nanozymes by CT26 cells was hindered in the presence of free HA molecules due to the competition of free HA molecules with nanozymes for the CD44 receptors of CT26 cells. Furthermore, compared to HCIP nanozymes, free IR820 molecules showed higher cellular uptake by CT26 cells, being ascribed to the different cellular internalization pathways between HCIP nanozymes (endocytosis) and free IR820 molecules (passive diffusion). Notably, the Cu^+ probe staining images revealed that CT26 cells incubated with HCIP or HCP nanozymes displayed a bright red fluorescence, whereas the cells treated with free IR820 molecules, HP or HIP nanoparticles showed weak red fluorescence similar to the control group (Fig. 6c). This indicates that Cu^{2+} ions released from the nanozymes confined within acidic organelles could be efficiently reduced by intracellular GSH to Cu^+ ions, which is beneficial for boosting CDT efficacy. The result is consistent with the acidity-triggered Cu^{2+} release of HCIP nanozymes and GSH-mediated Cu^{2+} reduction as presented in Fig. 3g and 5i, respectively. Next, the intracellular GSH-depleting ability of HCIP nanozymes was assessed by the DTNB assay. Without NIR laser irradiation, the intracellular GSH level of CT26 cells receiving free IR820 molecules was similar to the control group, suggesting that free IR820 molecules were not able to consume GSH (Fig. 6d). By contrast, the intracellular GSH level of CT26 cells treated with HP and HIP nanoparticles was somewhat reduced due to PDA-mediated GSH depletion. Note that HCP- or HCIP nanozyme-treated CT26 cells showed visibly declined GSH levels, signifying that combining PDA with Cu^{2+} could amplify GSH depletion. This result corresponds well to that presented in Fig. 5g. More importantly, with NIR laser irradiation, the intracellular GSH level of CT26 cells treated with HIP nanoparticles, HCP, or HCIP nanozymes was largely declined compared to that of cells receiving HP nanoparticles. These findings strongly demonstrate that the photothermal effect can further promote PDA-elicited and Cu^{2+}-mediated GSH exhaustion, and the $^1O_2$ produced by the IR820-involved photodynamic effect can oxidize GSH into GSSG.

3.6. *Intracellular ROS generation, mitochondrial damage, and LPO production*

To assess the ability of HCIP nanozymes in decomposing endogenous H_2O_2 to generate ·OH and converting O_2 into $^1O_2$, DCFH-DA was utilized to measure intracellular ROS level (Fig. 7a). Without NIR irradiation, no significant DCF fluorescence in CT26 cells incubated with free IR820 molecules and HIP nanoparticles was observed, similar to the control group (Fig. 7a and b). In contrast, visible DCF fluorescence signals of CT26 cells receiving HCIP nanozymes were attained, signifying the generation of intracellular·OH via the Fenton-like reaction between Cu^{2+}/Cu^+ redox couple and endogenous H_2O_2. Notably, with 808 nm NIR laser irradiation, CT26 cells incubated with HCIP nanozymes exhibited the strongest DCF fluorescence among cells receiving various treatments. Obviously, for HCIP nanozymes under laser irradiation, the increased ·OH production by hyperthermia-enhanced Fenton reaction combined with the production of $^1O_2$ from IR820-mediated photodynamic activity remarkably raised intracellular ROS level with the assistance of PDA/Cu^{2+}-induced GSH depletion (Scheme 1b). In contrast, with NIR laser irradiation, the endocytosed HCP nanozymes only generated limited ROS (·OH) via the Fenton-like reaction, and the Cu^{2+}-free HIP nanoparticles and free IR820 produced finite $^1O_2$ upon single IR820-elicited photodynamic effect.

Numerous studies have shown that mitochondrial damage is a key characteristic of ROS-associated apoptosis [52,53]. To measure the change of mitochondrial transmembrane potential provoked by HCIP nanozymes, the JC-1 staining assay was adopted. Intact mitochondria have a high transmembrane potential to induce red fluorescent JC-1 aggregates in the cells. In contrast, injured mitochondria display low transmembrane potential to cause green fluorescent JC-1 monomers to disperse in the cells [1,7]. As presented in Fig. 7c, without NIR laser irradiation, CT26 cells incubated with HCIP nanozymes exhibited

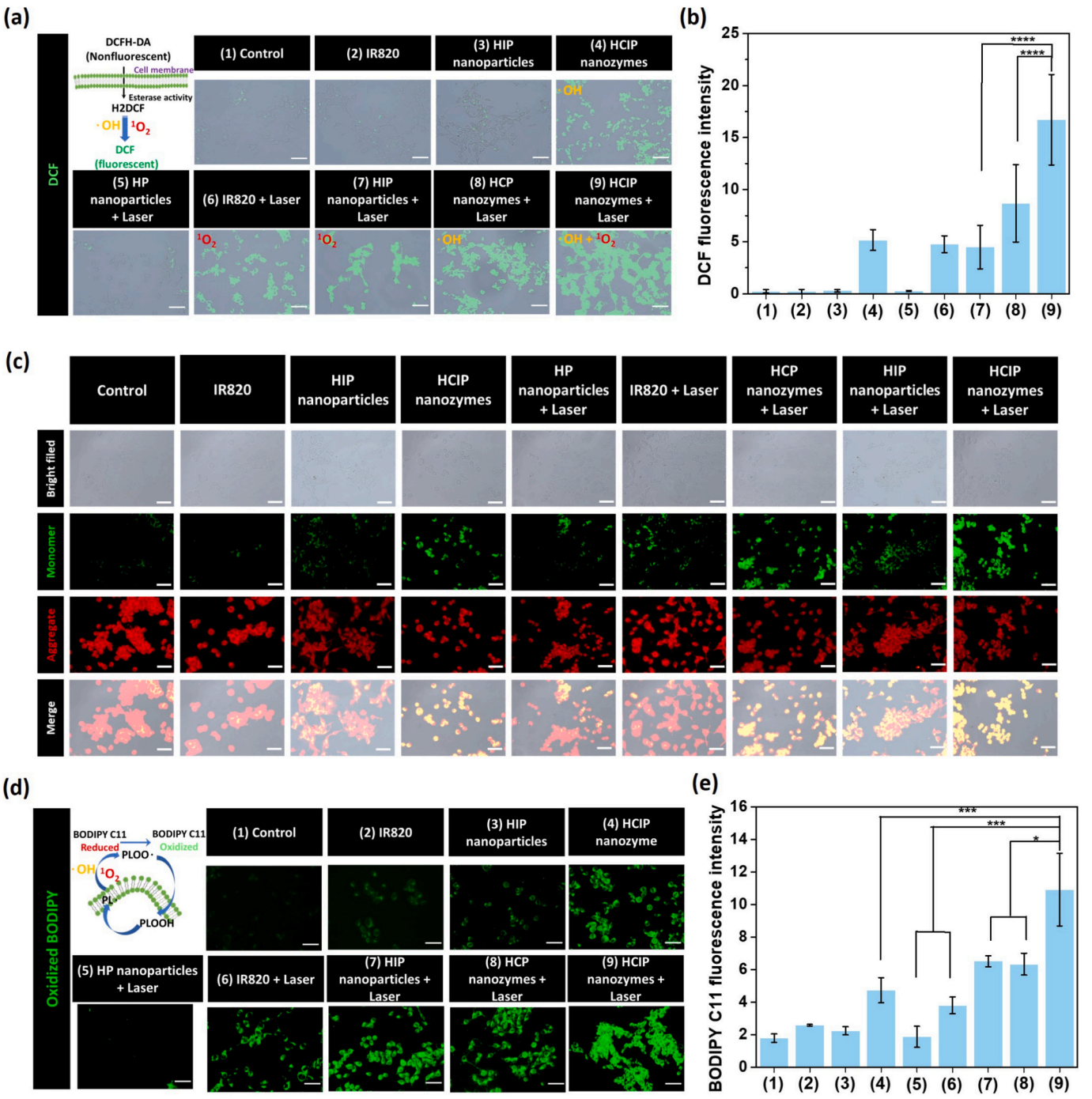

Fig. 7. (a) DCF fluorescence images and (b) quantification data of CT26 cells treated with various formulations receiving laser irradiation or not (1.0 W/cm^2, 5 min) (n = 3). Scale bars: 50 μm. (c) JC-1 staining of CT26 cells subjected to different treatments. Scale bars are 50 μm. (d) BODIPY$^{581/591}$ staining and (e) quantification data of CT26 cells receiving different treatments (n = 3). Scale bars are 50 μm.

somewhat higher green fluorescence than the control, free IR820, and HIP groups. This indicates that the HCIP nanozymes could generate moderate·OH to harm mitochondria. After NIR laser irradiation, the HCIP nanozymes-treated CT26 cells showed prominently enhanced green fluorescence among these treated cell groups. Only some green fluorescence was found in CT26 cells incubated with HCP nanozymes or HIP nanoparticles. Furthermore, no significant green fluorescence was observed in CT26 cells treated with HP nanoparticles plus NIR laser irradiation. These findings demonstrate that massive ·OH and $^1O_2$ produced from the intracellular HCIP nanozymes under NIR laser irradiation could effectively destroy mitochondria, whereas the finite·OH and $^1O_2$ provided by HCP nanozymes and HCP nanoparticles, respectively, cause limited mitochondria damage. Furthermore, only somewhat injured mitochondria were attained for CT26 cells treated with free IR820 molecules and NIR laser irradiation, ascribed to insufficient intracellular $^1O_2$ accumulation due to GSH-induced ROS exhaustion.

Increased studies showed that ferroptosis, a type of programmed cell death dependent on iron, was elicited by intracellular LPO accumulation due to excess ROS generation [7,18,54]. To examine the LPO production in CT26 cells treated with HCIP nanozymes, the BODIPY$^{581/591}$ as an LPO indicator was employed (Fig. 7d). Markedly, after NIR laser irradiation, CT26 cells treated with HCIP nanozymes showed the highest

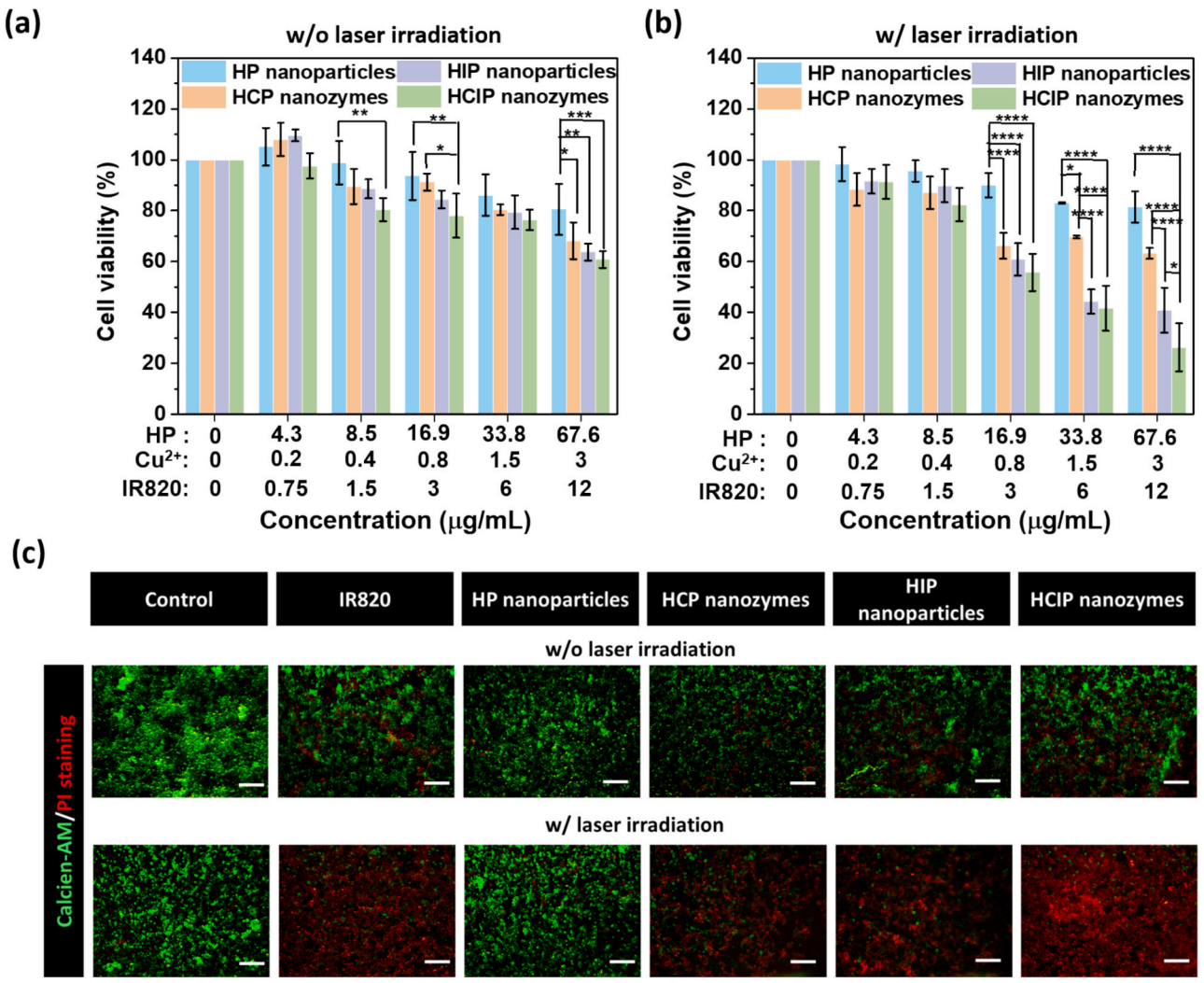

Fig. 8. Cell viability of CT26 cells exposed to different formulations without (a) or with (b) laser irradiation (n = 3). (c) Calcein-AM/PI-staining of CT26 cells receiving various treatments.

green fluorescence intensity compared to cells incubated with free IR820 molecules, HCP nanozymes, or HIP nanoparticles (Fig. 7d and e). Without NIR laser irradiation, the green fluorescence signals of CT26 cells incubated with HCIP nanozymes were higher than those of cells receiving IR820 molecules or HIP nanoparticles. These findings suggest that the HCIP nanozymes efficiently promote the intracellular accumulation of toxic LPO by NIR-activated $^1O_2$ production in combination with Cu^{2+}/Cu^{+}-mediated ·OH generation. In contrast, $^1O_2$ or ·OH alone generated from HIP nanoparticles or HCP nanozymes cannot produce sufficient intracellular LPO, while free IR820 molecules only lead to limited LPO generation owing to inadequate intracellular $^1O_2$. Because of these results, it was expected that the endocytosed HCIP nanozymes exposed to NIR irradiation could effectively provoke ferroptosis through massive LPO generation to enhance the anticancer effect (Scheme 1b).

3.7. *In vitro anticancer performance*

Encouraged by the prominent intracellular ROS generation, mitochondrial injury, and LPO production of HCIP nanozymes, their anticancer performance on CT26 cells was further studied. As a control, CT26 cells co-cultured with HP nanoparticles in the concentration range of 4.2–67.6 μg/mL, without NIR laser irradiation, maintained high viability of over 80 % (Fig. 8a), indicating negligible toxicity of HP nanoparticles on cancer cells. On the other hand, without NIR laser irradiation, compared to the IR820-treated CT26 cells showing reduced cell viability from 95 to 53 % with increased IR820 concentration (Fig. S8a), CT26 cells incubated with HIP nanoparticles maintained cell viability beyond 60 %. This indicates that the HP nanoparticles as IR820 vehicles could somewhat lower the IR820 dark cytotoxicity through acidity-controlled drug release. Through Cu^{2+}-elicited CDT, the HCP and HCIP nanozymes exhibited appreciable Cu^{2+} concentration-dependent cytotoxicity on CT26 cells. Notably, no significant death of normal WS1 cells, human skin fibroblast cells, incubated with HCIP nanozymes without NIR laser irradiation, was attained (Fig. S8b). The results suggest that the HCIP nanozymes diminished the toxicity of Cu^{2+} and IR820 in healthy cells, thanks to their selective CD44-targeting ability and the low intracellular H_2O_2 concentration in normal cells. After laser irradiation, CT26 cells alone maintained high viability (>95 %), comparable to cells without irradiation, indicating that laser exposure alone did not cause cellular damage. With laser irradiation, the viability of CT26 cells incubated with HCIP nanozymes was markedly decreased compared to that of cells receiving HCP nanozymes or HIP nanoparticles (Fig. 8b). Also, as presented in the live/dead cell staining images (Fig. 8c), the HCIP nanozyme-treated CT26 cells with laser irradiation showed more PI staining than those receiving other treatments. Given the above findings, the HCIP nanozymes effectively inhibited the proliferation of CT26 cells upon NIR-triggered hyperthermia and ROS storm combined with ferroptosis. In contrast, the single

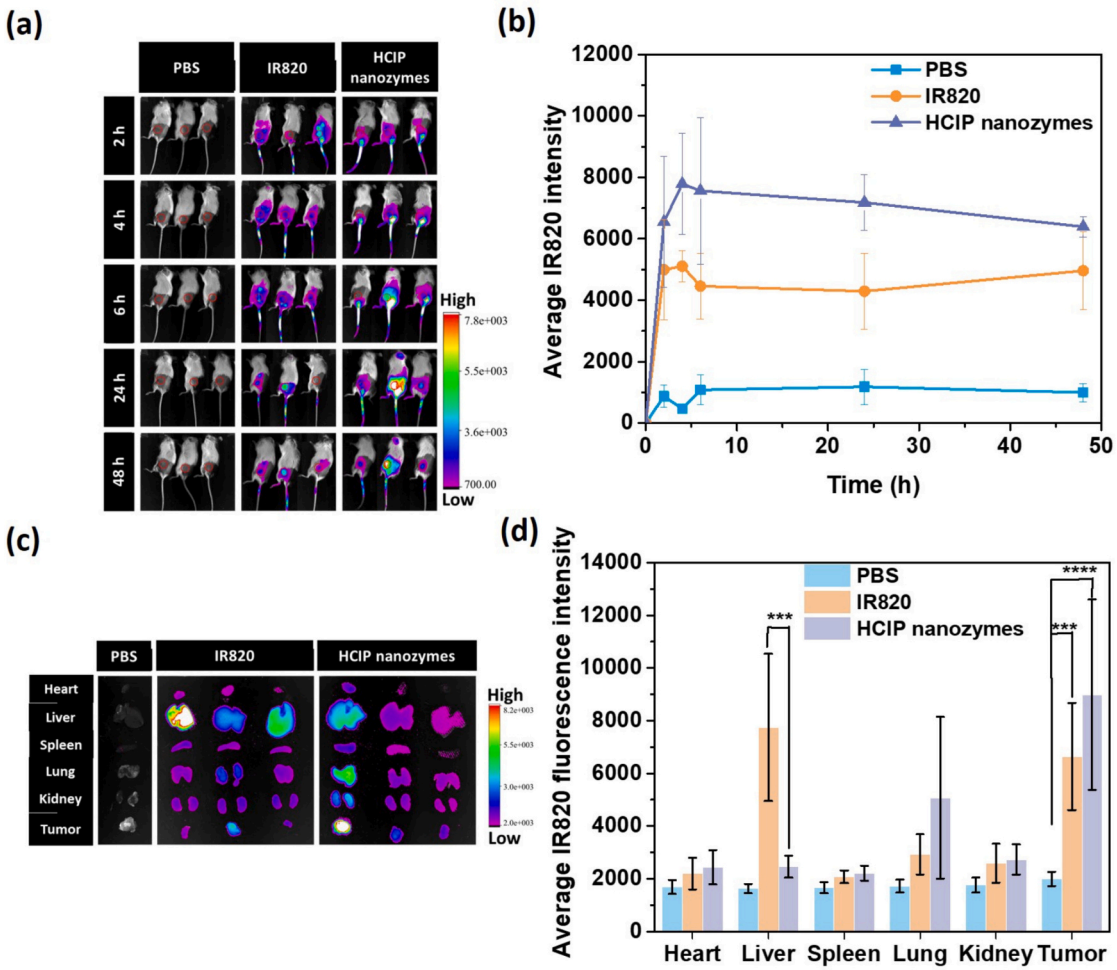

Fig. 9. (a) In vivo IR820 fluorescence images and (b) intensity quantification data of CT26 tumor-bearing mice with intravenous injection of PBS, IR820 molecules, or HCIP nanozymes (n = 3). The tumor regions were labeled with red circles. (c) Ex vivo IR820 fluorescence images and (d) fluorescence intensities of harvested tumors and major organs at 48 h post-injection with PBS, IR820 molecules, and HCIP nanozymes, respectively (n = 3). (For interpretation of the references to colour in this figure legend, the reader is referred to the web version of this article.)

Cu^{2+}-triggered CDT or IR820-based phototherapy delivered by HCP nanozymes or HIP nanoparticles only achieved limited anticancer efficacy. Furthermore, under laser irradiation, HCIP nanozymes exhibited lower cytotoxicity toward PC9 cells compared to CT26 cells (Fig. S8c), which can be attributed to the lower CD44 expression in PC9 cells, leading to reduced nanozyme internalization.

3.8. *In vivo biodistribution*

To evaluate the capability of HCIP nanozymes in targeting CD44-overexpressing tumors, their in vivo biodistribution was assessed with CT26 tumor-bearing mice. After tail-vein injection with free IR820 and HCIP nanozymes, the in vivo IR820 fluorescence imaging of the treated CT26 tumor-bearing mice was monitored by an IVIS imaging system. As presented in Figs. 9a and b, compared to the control and free IR820 group, the HCIP nanozyme group showed remarkably increased IR820 fluorescence signals in the tumor sites. Moreover, at 48 h post-injection, the HCIP nanozyme group exhibited an appreciably higher IR820 fluorescence intensity in tumor tissues compared to the liver and spleen, whereas the opposite trend was observed in the IR820 group (Fig. 9c and d). These data suggest that the hydrophilic HA-constituted surfaces and robust colloidal stability of HCIP nanozymes could reduce the capture of nanozymes by the RES-rich liver and spleen, thus promoting their deposition in tumor regions via the EPR effect and CD44-targeting performance. In contrast, amphiphilic IR820 molecules tend to aggregate into large particles during blood circulation, thus leading to massive accumulation in the liver rather than the tumor [39,55]. The blood compatibility of HCIP nanozymes was evaluated through an in vitro hemolysis assay. As presented in Fig. S9, no significant hemolysis was observed for HP nanoparticles and HCIP nanozymes. It was found that the red blood cells incubated with a high dose of HCIP nanozymes (100 μg/mL) still maintained a negligible hemolysis rate (less than 2 %). These results indicate that HCIP nanozymes have good blood compatibility, making them a safe candidate for intravenous administration.

3.9. *Suppression of in vivo tumor growth by synergistic therapy*

To confirm the hyperthermia-generating performance of HCIP nanozymes accumulated within tumor sites, the tumor temperature variation of tumor-bearing mice receiving intravenous injection of HCIP nanozymes and laser irradiation at 4 h post-injection was measured by an IR thermal imaging camera (Fig. 10a). During laser irradiation for 5 min, the HCIP nanozyme group and HIP nanoparticle group showed appreciably higher tumor temperature than the HCP nanozyme group and free IR820 group (Fig. 10b and c). This indicates that combining PDA-mediated and IR820-based photothermal effects elicited by HCIP nanozymes or HIP nanoparticles could effectively heat tumors. By contrast, the HCP nanozymes only caused insufficient tumor hyperthermia due to the sole reliance on PDA-induced photothermal properties. For the free IR820 group, the limited tumor accumulation and low

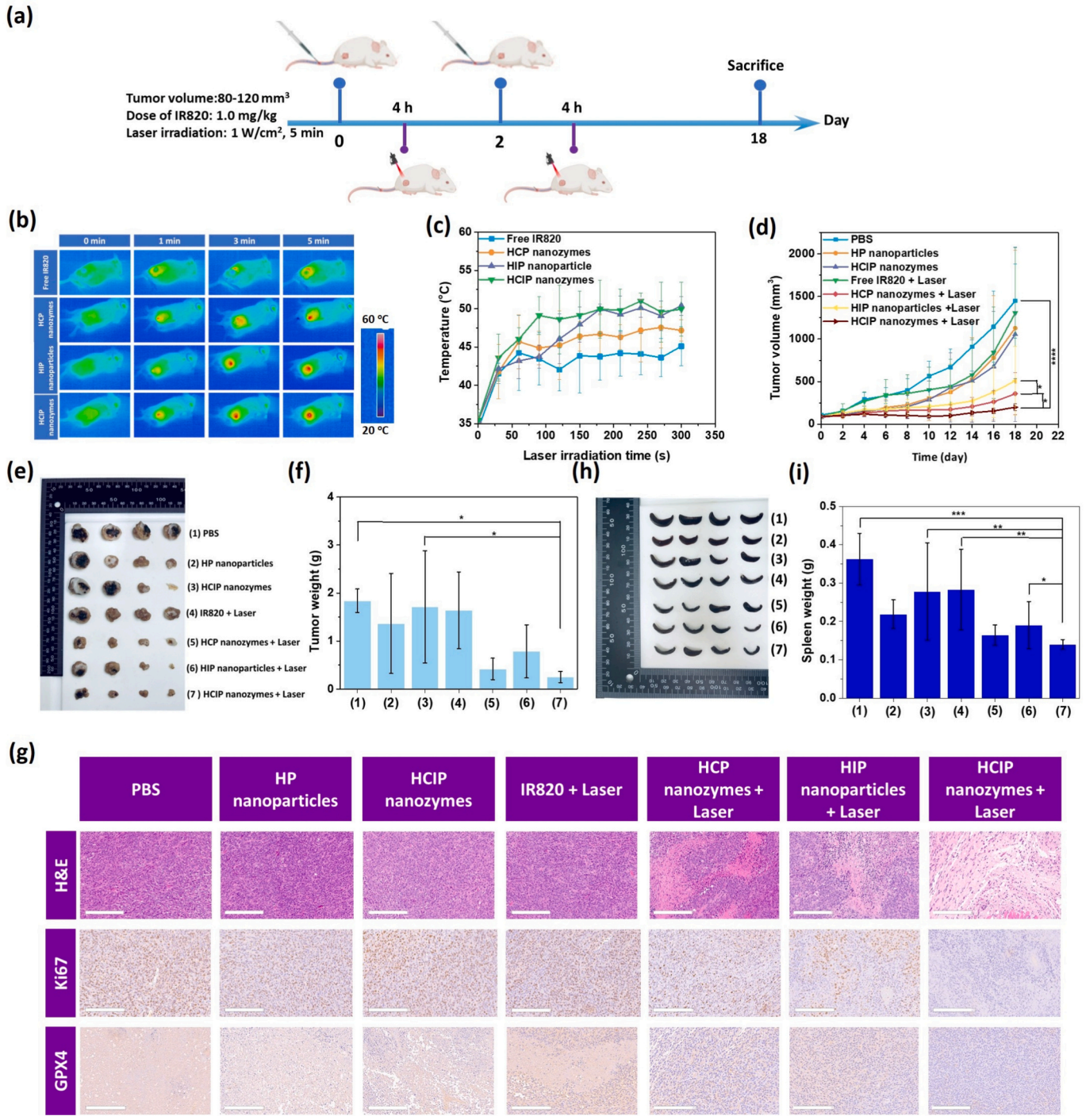

Fig. 10. (a) Scheme of the in vivo tumor growth inhibition test. (b) Thermal images and (c) temperature change curves of the tumors of CT26 tumor-bearing mice receiving different formulations during laser irradiation ($n = 4$). (d) Tumor volume variation curves of CT26 tumor-bearing mice subjected to various treatments (n = 4). (e) Photos and (f) weights of the tumors attained from the euthanized mice after the end of treatment (n = 4). (g) H&E, Ki-67, and GPX4 staining of tumor slides from CT26 tumor-bearing mice subjected to various treatments. Scale bars are 200 μm. (h) Photos and (i) weights of spleen harvested from the sacrificed mice after treatment (n = 4).

photothermal conversion efficiency of IR820 significantly hindered the temperature elevation within tumors.

Next, CT26 tumor-bearing mice were randomly assigned to seven groups: PBS control group, HP nanoparticle group, HCIP nanozyme group, IR820 + laser group, HCP nanozymes + laser group, HIP nanoparticles + laser group, and HCIP nanozymes + laser group to explore the in vivo antitumor potency. After 18-day treatment, without laser irradiation, the HP nanoparticle group and HCIP nanozyme group showed appreciably enlarged tumor volume comparable to the PBS group, revealing the failure of inhibiting tumor growth (Fig. 10d). Also, a visible tumor progression was observed in the IR820 + laser group. In contrast, with laser irradiation, the administration of HCP nanozymes, HIP nanoparticles, or HCIP nanozymes remarkably suppressed tumor growth, especially for HCIP nanozymes. Moreover, significant tumor shrinkage was observed in CT26 tumor-bearing mice receiving the HCIP nanozymes and laser irradiation (Fig. S10). Corresponding to the above

tumor growth inhibition results, the ex vivo studies showed that the HCIP nanozymes + laser group exhibited the smallest tumor size and weight compared to other treatment groups (Fig. 10e and f). More severe tumor tissue damage, cell apoptosis, and necrosis were observed in the H&E staining of tumor slices from the HCIP nanozymes + laser group than in other groups (Fig. 10g). As presented in the Ki67 staining of tumor slices, the HCIP nanozymes + laser group exhibited the lowest Ki67 staining, illustrating the prominent inhibitory ability on CT26 cell proliferation. More importantly, compared to PBS, HP nanoparticles, HCIP nanozyme groups, the HCP nanozymes + laser group, HIP nanoparticles + laser group, and HCIP nanozymes + laser group showed remarkably reduced GPX4 expression of tumor slices, in particular for the HCIP nanozymes + laser group. Undoubtedly, with laser irradiation, the HCIP nanozymes achieved potent hyperthermia-enhanced PDA/Cu^{2+}-mediated GSH depletion and $^1O_2$-elicited GSH oxidation, leading to the marked GPX4 down-regulation. The GPX4 inactivation of cancer cells has been verified to decrease their ROS-scavenging capability, thereby causing intracellular LPO deposition to provoke ferroptosis [56,57]. Based on the above findings, it is concluded that the HCIP nanozymes effectively retard tumor growth through NIR-triggered strong hyperthermia and ROS storm integrated with ferroptosis. In contrast, the combination of hyperthermia with CDT or PDT using HCP nanozymes or HIP nanoparticles exhibited only limited antitumor efficacy. Interestingly, under laser irradiation, while the in vitro anticancer efficacy of HIP nanoparticles was superior to that of HCP nanozymes (Fig. 8b), their in vivo antitumor effectiveness was slightly lower than that of HCP nanozymes. This could be attributed to that the tumor hypoxia unavoidably declined $^1O_2$ production of HIP nanoparticles to diminish the PDT performance, thus reducing the ROS-based antitumor effect.

On the other hand, the spleen, the largest lymphoid organ, plays a key role in maintaining homeostasis and immune response. Several studies report that spleen enlargement (splenomegaly) occurs in the advanced stages of cancer, indicating systemic inflammation and cancer progression [58,59]. As shown in Fig. 10h and i, the HCIP nanozymes + laser group displayed minimized splenomegaly and the lowest spleen weight compared to other treatment groups. Also, the microstructure of the spleen in the failed treatment groups analyzed by H&E staining was appreciably changed with disorganized red/white pulp with a non-specific mantle zone (Fig. S11). The HCIP nanozymes + laser group presented an organized microstructure with red/white pulp with a specific mantle zone. These results suggest that the HCIP nanozymes can effectively reduce splenomegaly through the outstanding NIR-triggered antitumor effect. Following treatment with HCIP nanozymes, the Cu^{2+} concentrations in tumors and major organs were measured using ICP-MS. As shown in Fig. S12, Cu^{2+} ions accumulated primarily in the liver and kidneys. However, the Cu^{2+} levels in all major organs and tumors remained below 0.005 ppm, suggesting efficient clearance of Cu^{2+} by the liver and kidneys. Note that the mice receiving various treatments had no significant variation in body weight during treatment, indicating that these therapeutic modalities employed in this work did not result in severe acute toxicity (Fig. S13). In addition to body weight monitoring, the H&E staining of the major organs from each group was conducted to assess the potential adverse effects of different treatments. All treatment groups showed no significant histopathological alterations in the heart, liver, lung, and kidney, suggesting that none of the treatments caused notable toxicity to these organs (Fig. S14).

4. Conclusion

Although PDA-based nanoparticles have been used to deliver either Cu^{2+} ions or photosensitizers [27,34], few studies have investigated the tumor-targeted co-delivery of Cu^{2+} ions and photosensitizers for synergistic cancer therapy. To boost the antitumor efficacy of ROS-mediated therapy based on catalytic therapy and PDT, we herein fabricated the HA-coated Cu^{2+}/IR820@PDA nanozymes capable of displaying tumor-specific photothermal-reinforced glutathione scavenging and ROS production. The nanozymes were characterized as solid, spherical shapes and exhibited a sound colloidal dispersion in a serum-containing solution. Moreover, the nanozymes showed acidity-activated Cu^{2+} and IR820 liberation, a robust photothermal conversion effect, and structural stability. With the assistance of PDA/Cu^{2+}-elicited GSH depletion, the photothermal nanozymes effectively produced ·OH and $^1O_2$ by Cu^{2+}-mediated Fenton reaction and IR820-based photodynamic effect. After being endocytosed by CT26 cells via CD44-mediated internalization, the nanozymes efficiently depleted GSH and generated massive ROS as well as hyperthermia under NIR laser irradiation, leading to mitochondrial damage and LPO to promote apoptosis and ferroptosis. Importantly, the nanozymes not only were remarkably deposited at the CT26 tumor tissues but also suppressed tumor growth and splenomegaly via photothermal-augmented ROS-mediated anticancer efficacy integrated with ferroptosis without severe adverse effects. This work offers a new perspective on boosting the antitumor effects of catalytic therapy and PDT, and will be promising in synergistic cancer therapy. Future studies will focus on evaluating the antitumor immune response of combination therapy and the long-term efficacy and safety of HCIP nanozymes in vivo.

CRediT authorship contribution statement

Hsiang-Yun Chih: Validation, Project administration, Methodology, Investigation, Formal analysis, Data curation. **I-Ju Liu:** Validation, Methodology, Investigation, Formal analysis. **Tzu-Chen Lin:** Visualization, Software, Investigation, Formal analysis. **Shang-Hsiu Hu:** Resources, Methodology, Investigation. **Tsai-Ching Hsu:** Supervision, Resources, Investigation, Funding acquisition. **Ju-An Liang:** Visualization, Resources, Methodology, Formal analysis. **Chia-Wei Kuo:** Visualization, Software, Resources, Formal analysis. **Bor-Show Tzang:** Writing – review & editing, Supervision, Resources, Investigation, Funding acquisition. **Wen-Hsuan Chiang:** Writing – review & editing, Writing – original draft, Supervision, Methodology, Investigation, Funding acquisition, Data curation, Conceptualization.

Declaration of competing interest

The authors declare that they have no known competing financial interests or personal relationships that could have appeared to influence the work reported in this paper.

Acknowledgements

This work is supported by the National Science and Technology Council (NSTC 113-2628-E-005-002-MY3 and NSTC 113-2622-E-005-017), National Chung Hsing University, and Chung Shan Medical University (NCHU-CSMU 11401), Taiwan.

Appendix A. Supplementary data

Supplementary data to this article can be found online at https://doi.org/10.1016/j.jcis.2025.139183.

Data availability

Data will be made available on request.

References

[1] N.P.N.S. Mehla, A. Begum, H.K. Chaturvedi, R. Ojha, C. Hartinger, M. Plebanski, S. K. Bhargava, Smart nanozymes for cancer therapy: the next frontier in oncology, Adv. Healthc. Mater. 12 (2023) e2300768.
[2] S. Koren, M. Bentires-Alj, Breast tumor heterogeneity: source of fitness, hurdle for therapy, Mol. Cell 60 (2015) 537–546.

[3] J. Zhang, X. Xu, H. Wei, D. Wu, L. Zeng, Pt/Pd dual-modified porphyrin metal-organic frameworks for NIR-II photothermal-enhanced photodynamic/catalytic therapy, J. Colloid Interface Sci. 678 (2025) 42–52.
[4] P. Lo, M. Rodríguez-Morgade, R. Pandey, D. Ng, T. Torres, F. Dumoulin, The unique features and promises of phthalocyanines as advanced photosensitisers for photodynamic therapy of cancer, Chem. Soc. Rev. 49 (2020) 1041–1056.
[5] H. Kang, S. Yu, R.M. Kim, Y. Kim, S.C. Shin, D. Jang, J.H. Han, S. Hong, E.E. Kim, S. H. Kim, D.J. Ahn, J.W. Han, S. Kim, K.T. Nam, L.P. Lee, D.H. Kim, Optically tunable catalytic cancer therapy using enzyme-like chiral plasmonic nanoparticles, Nat. Commun. 16 (2025) 2562.
[6] W.B. Direrssa, G. Getachew, A. Wibrianto, A.S. Rasal, V.S. Gurav, M. Zakki Fahmi, J. Y. Chang, Molybdenum-oxo-sulfide quantum dot-based nanocarrier: efficient generation of reactive oxygen species via photo/chemodynamic therapy and stimulus-induced drug release, J. Colloid Interface Sci. 647 (2023) 528–545.
[7] Y. Li, W. Fan, X. Gu, S. Liu, T. He, S. Gou, W. Meng, M. Li, X. Liu, Y. Ren, C. Qi, K. Cai, Biodegradable ferric phosphate nanocarriers with tumor-specific activation and glutathione depletion for tumor self-enhanced ferroptosis and chemotherapy, Adv. Funct. Mater. 34 (2024) 2313540.
[8] A.R. Sarkar, N. Mukherjee, A.K. Sarkar, N.R. Jana, Designing nano-hemin for ferroptosis-mediated cell death via enzymatic hemin digestion, ACS Appl. Mater. Interfaces 16 (2024) 64628–64637.
[9] J. Liu, Y. Yuan, Y. Cheng, D. Fu, Z. Chen, Y. Wang, L. Zhang, C. Yao, L. Shi, M. Li, C. Zhou, M. Zou, G. Wang, L. Wang, Z. Wang, Copper-based metal-organic framework overcomes cancer chemoresistance through systemically disrupting dynamically balanced cellular redox homeostasis, J. Am. Chem. Soc. 144 (2022) 4799–4809.
[10] N. Mehrotra, K. Pal, One-pot synthesis of tumor-targeted gold-doped $Cu_{1.92}S$ plasmonic nanodots for enhanced NIR-triggered, pH-responsive PTT/PDT/CDT, ACS Appl. Mater. Interfaces 17 (2025) 408–418.
[11] A. Deshwal, R.M. Tripathi, Palladium-powered nanozymes: a paradigm shift in precision medicine, Chem. Eng. J. 522 (2025) 168043.
[12] S. Wang, G. Yu, W. Yang, Z. Wang, O. Jacobson, R. Tian, H. Deng, L. Lin, X. Chen, Photodynamic-chemodynamic cascade reactions for efficient drug delivery and enhanced combination therapy, Adv. Sci. 8 (2021) 2002927.
[13] Y. Bai, M. Liu, X. Wang, K. Liu, X. Liu, X. Duan, Multifunctional nanoparticles for enhanced chemodynamic/photodynamic therapy through a photothermal, H_2O_2-elevation, and GSH-consumption strategy, ACS Appl. Mater. Interfaces 15 (2023) 55379–55391.
[14] A. Ghosh, A. Singh, S. Guha, B. Saha, G. Das, S.K. Sahu, A multifunctional NIR responsive upconversion porphyrin nanoprobe for Fenton/FRET induced ROS amplification and targeted drug delivery, J. Colloid Interface Sci. 700 (2025) 138311.
[15] M. Warszyńska, P. Repetowski, J.M. Dąbrowski, Photodynamic therapy combined with immunotherapy: recent advances and future research directions, Coord. Chem. Rev. 495 (2023) 215350.
[16] K. Moloudi, H. Abrahamse, B.P. George, Nanotechnology-mediated photodynamic therapy: focus on overcoming tumor hypoxia, Wiley Interdiscip. Rev. Nanomed. Nanobiotechnol. 16 (2024) e1937.
[17] Z. Liu, S. Liu, B. Liu, Y. Bian, M. Yuan, C. Yang, Q. Meng, C. Chen, P. Ma, J. Lin, Fe (III)-naphthazarin metal-phenolic networks for glutathione-depleting enhanced ferroptosis-apoptosis combined cancer therapy, Small 19 (2023) e2207825.
[18] K.A. Liang, H.Y. Chih, I.J. Liu, N.T. Yeh, T.C. Hsu, H.Y. Chin, B.S. Tzang, W. H. Chiang, Tumor-targeted delivery of hyaluronic acid/polydopamine-coated Fe^{2+}-doped nano-scaled metal-organic frameworks with doxorubicin payload for glutathione depletion-amplified chemodynamic-chemo cancer therapy, J. Colloid Interface Sci. 677 (2025) 400–415.
[19] Q.T. Hoang, V. Ravichandran, T.G.N. Cao, J.H. Kang, Y.T. Ko, T.I. Lee, M.S. Shim, Piezoelectric au-decorated ZnO nanorods: ultrasound-triggered generation of ROS for piezocatalytic cancer therapy, Chem. Eng. J. 435 (2022) 135039.
[20] A. Kashtiaray, M. Karimi, M. Ghafori-Gorab, A. Maleki, A comprehensive review on the recent applications of nanozymes in breast cancer therapy and diagnosis, Mater. Adv. 6 (2025) 3017–3042.
[21] N. Alizadeh, A. Salimi, Multienzymes activity of metals and metal oxide nanomaterials: applications from biotechnology to medicine and environmental engineering, J. Nanobiotechnol. 19 (2021) 26.
[22] Q. Weng, H. Sun, C. Fang, F. Xia, H. Liao, J. Lee, J. Wang, A. Xie, J. Ren, X. Guo, F. Li, B. Yang, D. Ling, Catalytic activity tunable ceria nanoparticles prevent chemotherapy-induced acute kidney injury without interference with chemotherapeutics, Nat. Commun. 12 (2021) 1436.
[23] M. Jannesari, O. Akhavan, H.R. Madaah Hosseini, B. Bakhshi, Oxygen-rich graphene/ZnO_2-ag nanoframeworks with pH-switchable catalase/peroxidase activity as O_2 nanobubble-self generator for bacterial inactivation, J. Colloid Interface Sci. 637 (2023) 237–250.
[24] A. Das, R.V.S. Uppaluri, S. Mitra, A review on waste derived carbon nanozyme: an emerging catalytic material for monitoring and degrading environmental pollutants, Chem. Eng. J. 507 (2025) 160762.
[25] M. Chen, X. Tong, Y. Sun, C. Dong, C. Li, C. Wang, M. Zhang, Y. Wen, P. Ye, R. Li, J. Wan, S. Liang, S. Shi, A ferroptosis amplifier based on triple-enhanced lipid peroxides accumulation strategy for effective pancreatic cancer therapy, Biomaterials 309 (2024) 122574.
[26] T. Soltani, B.K. Lee, Enhanced formation of sulfate radicals by metal-doped $BiFeO_3$ under visible light for improving photo-Fenton catalytic degradation of 2-chlorophenol, Chem. Eng. J. 313 (2017) 1258–1268.
[27] N. Xu, A. Hu, X. Pu, J. Wang, X. Liao, Z. Huang, G. Yin, Cu-chelated polydopamine nanoparticles as a photothermal medium and “immunogenic cell death” inducer for combined tumor therapy, J. Mater. Chem. B 10 (2022) 3104–3118.
[28] E. Falcone, A.G. Ritacca, S. Hager, H. Schueffl, B. Vileno, Y. El Khoury, P. Hellwig, C.R. Kowol, P. Heffeter, E. Sicilia, P. Faller, Copper-catalyzed glutathione oxidation is accelerated by the anticancer thiosemicarbazone Dp44mT and further boosted at lower pH, J. Am. Chem. Soc. 144 (2022) 14758–14768.
[29] J. Bonet-Aleta, M. Sancho-Albero, J. Calzada-Funes, S. Irusta, P. Martin-Duque, J. L. Hueso, J. Santamaria, Glutathione-triggered catalytic response of copper-iron mixed oxide nanoparticles. Leveraging tumor microenvironment conditions for chemodynamic therapy, J. Colloid Interface Sci. 617 (2022) 704–717.
[30] N. Losada-Garcia, A. Jimenez-Alesanco, A. Velazquez-Campoy, O. Abian, J. M. Palomo, Enzyme/nanocopper hybrid nanozymes: modulating enzyme-like activity by the protein structure for biosensing and tumor catalytic therapy, ACS Appl. Mater. Interfaces 13 (2021) 5111–5124.
[31] M.H. Hsieh, T.H. Wang, S.H. Hu, T.C. Hsu, J.L. Yow, B.S. Tzang, W.H. Chiang, Tumor site-specific PEG detachment and active tumor homing of therapeutic PEGylated chitosan/folate-decorated polydopamine nanoparticles to augment antitumor efficacy of photothermal/chemo combination therapy, Chem. Eng. J. 446 (2022) 137243.
[32] J. Xiao, L. Hai, Y. Li, H. Li, M. Gong, Z. Wang, Z. Tang, L. Deng, D. He, An ultrasmall Fe_3O_4-decorated polydopamine hybrid nanozyme enables continuous conversion of oxygen into toxic hydroxyl radical via GSH-depleted cascade redox reactions for intensive wound disinfection, Small 18 (2022) 2105465.
[33] M. Emanet, M.C. Lefevre, M.C. Ceccarelli, M. Battaglini, A. Carmignani, F. Schiavone, A. Marino, D. De Pasquale, M. Prato, F. De Boni, A. Petretto, M. Bartolucci, F. Catalano, S. Moscato, G. Ciofani, Polydopamine nanoparticle-based combined chemotherapy and photothermal therapy for the treatment of liver cancer, ACS Appl. Mater. Interfaces 16 (2024) 40695–40713.
[34] H. Hu, X. Liu, J. Hong, N. Ye, C. Xiao, J. Wang, Z. Li, D. Xu, Mesoporous polydopamine-based multifunctional nanoparticles for enhanced cancer phototherapy, J. Colloid Interface Sci. 612 (2022) 246–260.
[35] T.H. Wang, M.Y. Shen, N.T. Yeh, Y.H. Chen, T.C. Hsu, H.Y. Chin, Y.T. Wu, B. S. Tzang, W.H. Chiang, Photothermal nanozymes to self-augment combination cancer therapy by dual-glutathione depletion and hyperthermia/acidity-activated hydroxyl radical generation, J. Colloid Interface Sci. 650 (2023) 1698–1714.
[36] T.C. Lin, I.J. Liu, H.Y. Chih, B.S. Tzang, J.A. Liang, C.W. Kuo, C.Y. Hung, T.C. Hsu, W.H. Chiang, Photothermal-enhanced ROS storm by hyaluronic acid-conjugated nanocatalysts to amplify tumor-specific photo-chemodynamic therapy and immune response, Int. J. Biol. Macromol. 309 (2025) 142975.
[37] P. Manivasagan, A. Joe, H.W. Han, T. Thambi, M. Selvaraj, K. Chidambaram, J. Kim, E.S. Jang, Recent advances in multifunctional nanomaterials for photothermal-enhanced Fenton-based chemodynamic tumor therapy, Mater. Today Bio. 13 (2022) 100197.
[38] W. Cao, J. Sui, M. Ma, Y. Xu, W. Lin, Y. Chen, Y. Man, Y. Sun, Y. Fan, X. Zhang, The preparation and biocompatible evaluation of injectable dual crosslinking hyaluronic acid hydrogels as cytoprotective agents, J. Mater. Chem. B 7 (2019) 4413–4423.
[39] G.R. Nirmal, Z.C. Lin, C.H. Lin, C.T. Sung, C.C. Liao, J.Y. Fang, Polydopamine/IR820 nanoparticles as topical phototheranostics for inhibiting psoriasiform lesions through dual photothermal and photodynamic treatments, Biomater. Sci. 10 (2022) 6172.
[40] X. Zhong, K. Yang, Z. Dong, X. Yi, Y. Wang, C. Ge, Y. Zhao, Z. Liu, Polydopamine as a biocompatible multifunctional nanocarrier for combined radioisotope therapy and chemotherapy of cancer, Adv. Funct. Mater. 25 (2015) 7327–7336.
[41] C.N. Schnell, G. Mertz, J. Hao, A.W. Van Vuure, A. Laachachi, C.A. Fuentes, Stable polydopamine-based suspension for scalable surface modification of bamboo fibre-reinforced composites, Compos. - A: Appl. Sci. Manuf. 199 (2025) 109206.
[42] D. Sprouse, Y. Jiang, J.E. Laaser, T.P. Lodge, T.M. Reineke, Tuning cationic block copolymer micelle size by pH and ionic strength, Biomacromolecules 17 (2016) 2849–2859.
[43] V.T.A. Nguyen, M.-C. De Pauw-Gillet, O. Sandre, M. Gauthier, Biocompatible polyion complex micelles synthesized from arborescent polymers, Langmuir 32 (2016) 13482–13492.
[44] S. Oe, K. Miyagawa, Y. Honma, M. Harada, Copper induces hepatocyte injury due to the endoplasmic reticulum stress in cultured cells and patients with Wilson disease, Exp. Cell Res. 347 (2016) 192–200.
[45] Y. Xiong, Z. Wang, Q. Wang, Q. Deng, J. Chen, J. Wei, X. Yang, X. Yang, Z. Li, Tumor-specific activatable biopolymer nanoparticles stabilized by hydroxyethyl starch prodrug for self-amplified cooperative cancer therapy, Theranostics 12 (2022) 944–962.
[46] J. Chang, W. Yin, H. Zhi, S. Chen, J. Sun, Y. Zhao, L. Huang, L. Xue, X. Zhang, T. Zhang, H. Dong, Y. Li, Copper deposition in polydopamine nanostructure to promote cuproptosis by catalytically inhibiting copper exporters of tumor cells for cancer immunotherapy, Small 20 (2024) e2308565.
[47] M. Saraf, R. Prateek, B. Ranjan, V.K. Balasubramaniam, R.K. Gupta Thakur, Polydopamine-enabled biomimetic surface engineering of materials: new insights and promising applications, Adv. Healthc. Mater. 11 (2024) 2300670.
[48] A. Bera, D. Bagchi, S.K. Pal, Improvement of photostability and NIR activity of cyanine dye through nanohybrid formation: key information from ultrafast dynamical studies, J. Phys. Chem. A 123 (2019) 7550–7557.
[49] S. Koo, O.K. Park, J. Kim, S.I. Han, T.Y. Yoo, N. Lee, T.G. Kim, H. Kim, C. Lim, J. S. Bae, J. Yoo, D. Kim, S.H. Choi, T. Hyeon, Enhanced chemodynamic therapy by cu-Fe peroxide nanoparticles: tumor microenvironment-mediated synergistic Fenton reaction, ACS Nano 16 (2022) 2535–2545.
[50] M. Luo, H. Yukawa, K. Sato, M. Tozawa, M. Tokunaga, T. Kameyama, T. Torimoto, Y. Baba, Multifunctional magnetic CuS/Gd_2O_3 nanoparticles for fluorescence/magnetic resonance bimodal imaging-guided photothermal-intensified

chemodynamic synergetic therapy of targeted tumors, ACS Appl. Mater. Interfaces 14 (2022) 34365–34376.
[51] Y.Y. Wang, X.Y. Zhang, S.L. Li, F.L. Jiang, P. Jiang, Y. Liu, AuPt-loaded cu-doped polydopamine nanocomposites with multienzyme-mimic activities for dual-modal imaging-guided and cuproptosis-enhanced photothermal/nanocatalytic therapy, Anal. Chem. 95 (2023) 14025–14035.
[52] F.R. Palma, B.N. Gantner, M.J. Sakiyama, C. Kayzuka, S. Shukla, R. Lacchini, B. Cunniff, M.G. Bonini, ROS production by mitochondria: function or dysfunction? Oncogene 43 (2024) 295–303.
[53] H. Nakamura, K. Takada, Reactive oxygen species in cancer: current findings and future directions, Cancer Sci. 112 (2021) 3945–3952.
[54] D. Tang, X. Chen, R. Kang, G. Kroemer, Ferroptosis: molecular mechanisms and health implications, Cell Res. 31 (2021) 107–125.
[55] T. Duong, X. Li, B. Yang, C. Schumann, H.A. Albarqi, O. Taratula, O. Taratula, Phototheranostic nanoplatform based on a single cyanine dye for image-guided combinatorial phototherapy, Nanomedicine 13 (2017) 955–963.
[56] N. Noguchi, Y. Saito, E. Niki, Lipid peroxidation, ferroptosis, and antioxidants, Free Radic. Biol. Med. 237 (2025) 228–238.
[57] F. Ursini, M. Maiorino, Lipid peroxidation and ferroptosis: the role of GSH and GPx4, Free Radic. Biol. Med. 152 (2020) 175–185.
[58] R.P.S.S.B. Alvi, N. Begum, B. Veeresh, A.K. Rengan, Self-assembled fluorosome-polydopamine complex for efficient tumor targeting and commingled photodynamic/photothermal therapy of triple-negative breast cancer, Biomacromolecules 22 (2021) 3926–3940.
[59] G.C. Tobias, J.L.P. Gomes, L.G. Fernandes, V.A. Voltarelli, N.R. de Almeida, P. R. Jannig, R.W.A. de Souza, C.E. Negrão, E.M. Oliveira, R. Chammas, C.R.R. Alves, P.C. Brum, Aerobic exercise training mitigates tumor growth and cancer-induced splenomegaly through modulation of non-platelet platelet factor 4 expression, Sci. Rep. 13 (2023) 21970.